Computational Mechanics (2021) 67:33–55
https://doi.org/10.1007/s00466-020-01918-x

ORIGINAL PAPER

A numerical study into element type and mesh resolution for crystal plasticity finite element modeling of explicit grain structures

William G. Feather[1] · **Hojun Lim**[2] · **Marko Knezevic**[1]

Received: 19 May 2020 / Accepted: 24 August 2020 / Published online: 10 September 2020

Abstract
A large number of massive crystal-plasticity-finite-element (CPFE) simulations are performed and post-processed to reveal the effects of element type and mesh resolution on accuracy of predicted mechanical fields over explicit grain structures. A CPFE model coupled with Abaqus/Standard is used to simulate simple-tension and simple-shear deformations to facilitate such quantitative mesh sensitivity studies. A grid-based polycrystalline grain structure is created synthetically by a phase-field simulation and converted to interface-conformal hexahedral and tetrahedral meshes of variable resolution. Procedures for such interface-conformal mesh generation over complex shapes are developed. FE meshes consisting of either hexahedral or tetrahedral, fully integrated as linear or quadratic elements are used for the CPFE simulations. It is shown that quadratic tetrahedral and linear hexahedral elements are more accurate for CPFE modeling than linear tetrahedral and quadratic hexahedral elements. Furthermore, tetrahedral elements are more desirable due to fast mesh generation and flexibility to describe geometries of grain structures.

Keywords Solids · Finite element methods · Plasticity · Micromechanics · Mesh sensitivity

1 Introduction

Modeling of polycrystalline metals often employs spatio-temporal domains of constituent grains interacting explicitly with each other, while achieving the state of stress equilibrium and strain compatibility [1–4]. Such modeling is referred to as full-field. The full-field microstructural modeling, especially in three-dimensions (3D), accounts for topological effects of microstructural evolution on micromechanical fields defined in term of stress and strain and facilitates better understanding of complex phenomena pertaining to material behavior. The stress equilibrium governing equations of mechanics in conjunction with a constitutive law describing the material behavior under deformation can be solved numerically using the finite element method (FEM) in terms of a work-conjugated stress–strain measures [2]. For the FEM, the microstructural domain must be discretized into finite elements. If a crystal plasticity-based constitutive law is embedded at every FE integration point, the mechanical fields are governed by crystallography including deformation mechanisms and crystal lattice orientation as well as the evolution of inter- and intra-granular misorientation, grain shape, and grain-boundary-character-distribution (GBCD).

Beginning from the research reported in [5], the crystal plasticity FE (CPFE) models have been extensively used to predict mechanical fields, typically with a sub-grain mesh resolution [6–11]. In early CPFE modeling, the morphology of grains has not been considered [12–18]. Subsequent studies have considered simplified geometries representing grains such as rhombic dodecahedrons, cuboids, and truncated octahedrons [19–21]. As these geometries were gross approximations of real grain structures and unable to represent grain boundaries, the intra-granular and inter-granular fields were also gross approximations [22]. Recent developments in the field have facilitated accurate representation of individual grains to elucidate the role of grain structure in determining heterogeneous deformation [9, 10, 23–30]. Such heterogeneous deformation as a function of microstructural evolution and inherent anisotropy even under uniform macroscopic deformation conditions can be predicted by CPFE models. The plasticity modeling at grain scale is essen-

✉ Marko Knezevic
marko.knezevic@unh.edu

[1] Department of Mechanical Engineering, University of New Hampshire, Durham, NH 03824, USA

[2] Department of Computational Materials and Data Science, Sandia National Laboratories, Albuquerque, NM 87185, USA

tial for understanding and attempting to predict mechanical extremes such as void nucleation driven by local strain concentrations. While full-field models can be used to obtain homogenized material response, more often mean-field models are used for such purpose. However, the mean field models do not account for explicit grain-to-grain interactions [31–44].

An essential building block pertaining to the CPFE modeling of explicit grain structure is generation of polycrystalline domain. To this end, voxel-based microstructures are converted into finite element meshes. One methodology to generate a synthetic voxel-based microstructure is the Voronoi tessellation [24, 25, 45–48]. A software, DREAM.3D (the digital microstructure analysis environment in 3D) has been developed by U.S. Air Force Research Laboratory and Blue Quartz as a more sophisticated tool to generate voxel-based microstructures [49]. Grain size and shape statistics, orientation and misorientation distributions can be used as inputs to generate voxel-based models of microstructure. A convenient output of the software for subsequent mesh generation is surface mesh over individual grains. Synthetic microstructures represented by voxels can further be obtained by microstructural evolution models such as phase-field grain growth [50], Potts (Monte-Carlo) grain growth [51, 52], and cellular automata [53, 54]. In addition to synthetic generation of voxel-based microstructures, several experimental techniques have been advanced/developed to acquire real 3D grain structure data. These techniques include, robotic serial sectioning complemented with electron backscattering diffraction (EBSD) [55, 56], focused ion beam (FIB) EBSD serial sectioning [57–62], and non-destructive near field high energy X-ray diffraction microscopy (nf HEDM) [63–67]. DREAM.3D offers various features to post-process such experimental data producing triangular surface mesh for grains for subsequent volume mesh generation.

In polycrystalline CPFE simulations, microstructural data is converted into a finite element mesh. A voxel grid-based description of the microstructure requires a significant number of voxels to capture the complex geometry of the grains accurately. If every voxel is converted to a hexahedral (brick) finite element [68], the mesh may contain a very large number of finite elements, increasing the computational cost of such simulations beyond practical levels. In addition, it is shown that voxelated meshes could develop artificial stress/strain localizations at interfaces or triple junctions due to stair-case instead of smooth/flat grain boundaries present in such meshes [28, 69]. In summary, while a microstructure obtained directly from experimental images in voxel format may be the easiest way to initialize simulations with hexahedral elements, large number of voxels equivalent to the number of hexahedral elements may make such simulations computationally inefficient and the intrinsic stair-stepped grain boundaries may make the simulations inaccurate.

In recent works [70, 71], we have developed procedures relying on the surface mesh of individual grain to create tetrahedral volume mesh, which is conformal between grains. The conformal mesh implies that neighboring grains share nodes at grain boundaries. Several subsequent works have utilized the developed tools to study shear band formation [72] and explicit twins [8, 73]. These procedures have also been advanced to create polycrystalline meshes for various specimen geometries other than cubes suitable for microforming [74, 75] and micromechanical testing [46] simulations. Also, mesh generation software package Cubit, developed at Sandia National Laboratories [76], can generate 3D interface conformal meshes using not only tetrahedral but also hexahedral elements.

In this work, we investigate effects of element types and mesh resolution for CPFE modeling of explicit grain structures. The study complements the recent work of mesh sensitivity of single crystal with grains represented by simple cubic shapes and polycrystalline representative volume elements while varying factors such as initial textures, hardening models and boundary conditions [27]. In addition to accounting for the effect from complex grain features in realistic microstructures, the present study considers four element types including linear tetrahedral (*tet*), quadratic tet, linear hexahedral (*hex or brick*), and quadratic hex of various resolutions in predicting the mechanical fields. A large number of massive CPFE simulations are performed and post-processed to reveal the effects of element type and mesh resolution on accuracy of predicted mechanical fields. An initial voxel-based polycrystalline grain structure (microstructural cell) is created synthetically by a phase field grain growth simulation and converted to interface-conformal hex and tet meshes at various levels of discretization. Considering that boundary conditions may affect the mesh sensitivity in addition to grain structure, two types of boundary conditions involving simple tension (ST) and simple shear (SS) are imposed over the microstructural domain for the given number of elements i.e. their degrees-of-freedom. Since these simulations require significant memory size and computational time, a parallel computing infrastructure is utilized. Comparisons of CPFE results in terms accuracy and computational efficiency are presented and discussed in the paper. It is anticipated that the main conclusion from this study will serve as useful guidance in polycrystalline CPFE modeling.

2 Modeling framework

2.1 Summary of CPFE and a hardening model

A standard single crystal elasto-visco-plastic constitutive law is used to relate a pair of work conjugated stress and strain measures at each integration point, in every finite element

[13]. This formulation is briefly summarized below. The total deformation gradient tensor, $\mathbf{F}$, at every integration point obtained from the finite element solver is multiplicatively decomposed into an elastic stretching and lattice rotation part, $\mathbf{F}^*$, and the plastic part, $\mathbf{F}^p$, embedding the plastic deformation carried out by crystallographic slip

$$\mathbf{F} = \mathbf{F}^*\mathbf{F}^p. \tag{1}$$

The stress–strain relations are

$$\mathbf{T}^* = \mathbf{C}\mathbf{E}^*, \mathbf{T}^* = \mathbf{F}^{*-1}\{(det\mathbf{F}^*)\boldsymbol{\sigma}\}\mathbf{F}^{*-T}, \mathbf{E}^* = \frac{1}{2}\left\{\mathbf{F}^{*T}\mathbf{F}^* - \mathbf{I}\right\}, \tag{2}$$

where $\mathbf{C}$ is the elastic stiffness tensor, $\mathbf{T}^*$ is the second Piola–Kirchhoff stress, $\mathbf{E}^*$ is the Green-Lagrangian strain tensors, and $\boldsymbol{\sigma}$ is the Cauchy stress. The flow rule for $\mathbf{F}^p$ is

$$\dot{\mathbf{F}}^p = \mathbf{L}^p\mathbf{F}^p, \mathbf{L}^p = \sum_\alpha \dot{\gamma}^\alpha \mathbf{b}_o^\alpha \otimes \mathbf{n}_o^\alpha, \tag{3}$$

where $\dot{\gamma}^\alpha$ is the shearing rate per slip system α, while $\mathbf{b}_o^\alpha$, and $\mathbf{n}_o^\alpha$ denote the slip system geometry i.e. the slip direction and the plane normal, respectively, in the total Lagrangian manner denoted by the subscript 'o'. The power-law relation is used for the shearing rate [77–79].

$$\dot{\gamma}^\alpha = \dot{\gamma}_0^\alpha \left(\frac{|\tau^\alpha|}{\tau_c^\alpha}\right)^{1/m} sign(\tau^\alpha), \tag{4}$$

where τ^α is on the driving force ($\tau^\alpha = \mathbf{T}^* \cdot \mathbf{b}_o^\alpha \otimes \mathbf{n}_o^\alpha$) on the slip system α, τ_c^α is the resistance to slip, $\dot{\gamma}_0^\alpha$ is a reference slip rate of 0.001 s^{-1}, and m is the strain rate sensitivity constant of 0.01. To complete the theory, the crystal lattice spin, $\mathbf{W}^*$, is

$$\mathbf{W}^* = \mathbf{W}^{app} - \mathbf{W}^p, \mathbf{W}^p = \frac{1}{2}\left(\mathbf{L}^p - \mathbf{L}^{pT}\right), \tag{5}$$

where $\mathbf{W}^{app}$ is the applied spin over the polycrystal and $\mathbf{W}^p$ is the plastic spin. The numerical implementation of the above theory is described in detail in [13].

The constitutive model summarized above has been coupled with a hardening model for the evolution of slip resistance. The model has been presented and applied to polycrystalline Cu in [7]. The model considers statistically stored dislocations (SSDs) governing the threshold stresses for the activation of each slip system. The densities of dislocations evolve based on a thermally activated rate law with shearing on slip systems [80]. The slip resistance, τ_c^α, for all $\{111\}\langle 110\rangle$ slip systems α, is the isotropic over all slip systems, i.e.,$\tau_c^\alpha = \tau_c, \forall\alpha$. However, it varies from grain to grain. The τ_c is the sum of three contributions as follows [81–85]

$$\tau_c = \tau_0 + \tau_{for} + \tau_{sub}, \tag{6}$$

with τ_0 being a friction stress that embeds the Peierls stress, barrier effect due to grain size, and any content of initial dislocation density. This term does not evolve with plastic strain but decays exponentially with temperature as is the case for many metals [38, 86].

$$\tau_0 = Aexp\left(-\frac{T-298}{B}\right). \tag{7}$$

here A and B are fitting constants and T is the temperature in K. The remaining two contributions to slip resistance are the forest and substructure/debris interaction stresses, τ_{for} and τ_{sub}, respectively. These two terms evolve with dislocation densities, i.e. the forest and substructure dislocation densities ρ_{for} and ρ_{sub} according to the Taylor-type relations [87–89].

$$\tau_{for} = \chi b\mu\sqrt{\rho_{for}}, \tag{8}$$

$$\tau_{sub} = 0.086\mu b\sqrt{\rho_{sub}}log\left(\frac{1}{b\sqrt{\rho_{sub}}}\right), \tag{9}$$

where b is the Burgers vector (2.5563×10^{-10} m for Cu), μ is the shear modulus (4.8×10^4 MPa for Cu) and χ is a dislocation interaction factor [90] that varies with temperature as follows.

$$\chi = \chi_0 - K_1 ln\left(\frac{T}{K_2}\right). \tag{10}$$

At room temperature, $\chi\,(T = 298K)$ is 0.9541. The initial density of statistically stored forest dislocation density is set to 10^{12} m^{-2}, which is an annealed state of the material and ρ_{for} is determined by the balance between the rate of generation and the rate of removal i.e. dynamic recovery [87, 91, 92],

$$\begin{aligned}\frac{\partial\rho_{for}}{\partial\gamma} &= \frac{\partial\rho_{gen,for}}{\partial\gamma} - \frac{\partial\rho_{rem,for}}{\partial\gamma}\\ &= k_1\sqrt{\rho_{for}} - k_2(\dot{\varepsilon}, T)\rho_{for},\\ \Delta\rho_{for} &= \frac{\partial\rho_{for}}{\partial\gamma}\sum_\alpha|\Delta\gamma^\alpha|,\end{aligned} \tag{11}$$

with k_1^s as a coefficient for statistical trapping and k_2^s as a rate-sensitive coefficient defined by

$$\frac{k_2}{k_1} = \frac{\chi b}{g}\left(1 - \frac{kT}{Db^3}ln\left(\frac{\dot{\varepsilon}}{\dot{\varepsilon}_o}\right)\right). \tag{12}$$

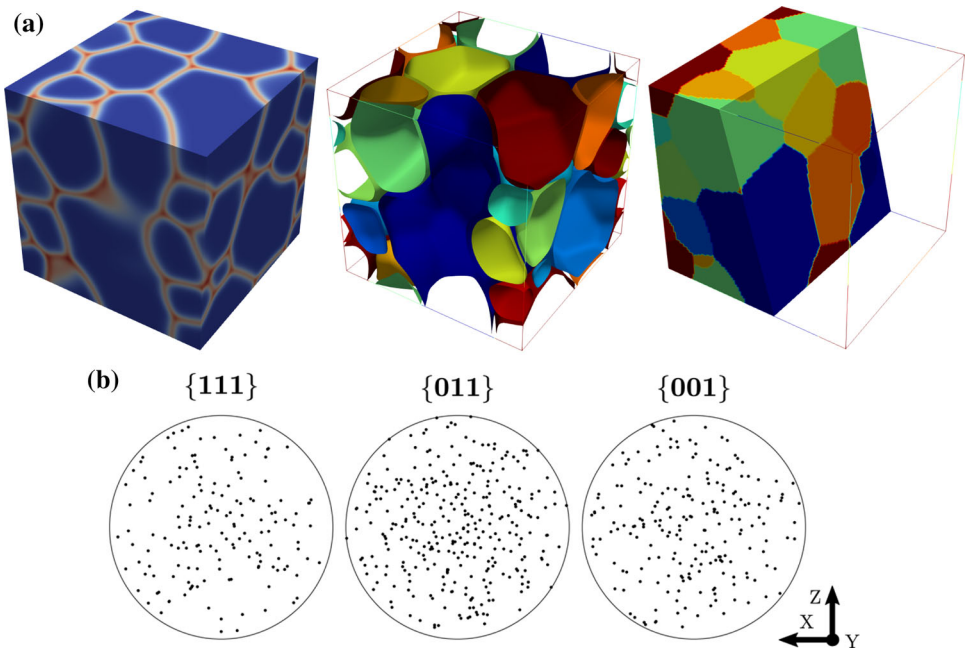

Fig. 1 **a** A microstructure produced using a phase field grain growth code. The original phase field data is shown on the left with red regions (grain boundary regions) representing locations where multiple phase fields exist. The middle image shows grain boundaries. The image on the right is a section through the microstructure showing the internal structure. **b** Pole figures showing the distribution of crystal orientations, which will be assigned to the model in **a**

In Eq. (12), k, $\dot{\varepsilon}_o$, g, and D are a Boltzmann constant, a reference strain-rate of 10^7 s^{-1}, an activation enthalpy, and a drag stress, respectively. The last two are fitting constants.

The rate of debris density of dislocations evolves using

$$\Delta\rho_{sub} = qb\sqrt{\rho_{sub}}k_2\rho_{for}\sum_{\alpha}\left|\Delta\gamma^{\alpha}\right|, \tag{13}$$

with q as a rate coefficient defined by

$$q = q_0 ln\left(1 + \frac{T}{q_1}\right). \tag{14}$$

The factor q determines a fraction of dislocations that leads to debris formation, while the rest is annihilated. Equation (13) is based on thermally activated processes, such as cross slip and climb, which are responsible for pattern formation [93–96]. In the model, a smaller fraction of the recovered forest dislocations contributes to debris formation.

The hardening law parameters for polycrystalline Cu have been presented in [7]. The parameters have been calibrated and validated to mechanical tests on Cu over a range of strain-rates and temperatures. However, only quasi-static deformation at room temperature is considered in the present work.

2.2 Mesh generation procedures

To generate an interface conformal hexahedral mesh of polycrystals, the Sculpt meshing tool [97, 98], a companion application to the Cubit Meshing and Geometry Toolkit developed at Sandia National Laboratories [76] is used. A phase field data of microstructure is used to define volume fractions of grains and locate the center of the grain interfaces (grain boundaries) at every grid. Cartesian grid nodes near the interfaces are moved to approximated grain interfaces from volume fractions and one or more hexahedra are inserted on both sides of the grain interfaces. A smoothing step is then performed to improve both smoothness of the interface planes and the quality of the hexahedra. More detailed description of interface conformal meshing procedures can be found in [28, 97].

The initial voxelated microstructure generated by a phase-field grain growth simulation is shown in Fig. 1a. The grain growth simulation was performed on a uniform grid of $96 \times 96 \times 96$ until approximately 50 grains were achieved. The simulation relied on a coarse-grained free energy functional of a polycrystalline system, which is solved for structural order parameters that describe individual grains. The spatio-temporal evolution of the order parameter was based on Allen–Cahn equation [99]. More detailed description of the model can be found in [28, 100, 101]. The snapshot of the microstructure is chosen to resolve interfaces/triple junctions of grains. Edge length of the cube is a unity. The voxels that make up the phase-field model create stair-stepped grain boundaries. If such hexahedral meshes with the stair-case grain boundaries are used in CPFE simulations, mechanical fields at the grain boundary regions are over predicted. Such differences in the local plasticity values between the stair-case and the smooth/flat grain boundaries have been studied in [69]. The work revealed that the grain boundaries represented by the stair-case morphology are sources for extreme plasticity and should be replaced with locally smooth/flat morphology.

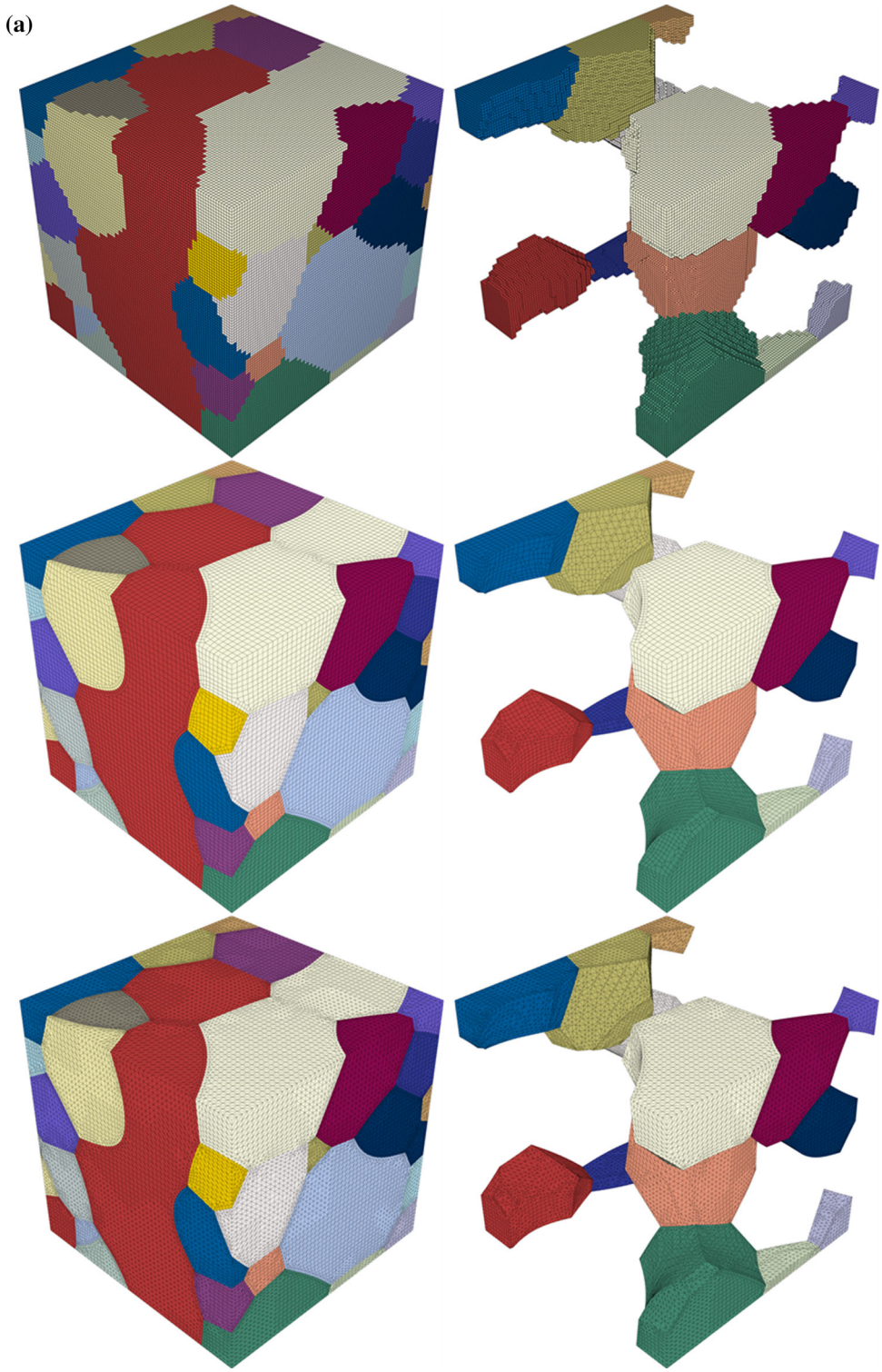

Fig. 2 **a** Polycrystalline microstructure consisting of 52 grains discretized into voxels, hexahedral elements, and tetrahedral elements. The images on the right show internal boundaries revealing the stair-stepped morphology of the grain boundary voxels in the voxel-based microstructure, which are smoothed to squares (hexahedral elements) and triangles (tetrahedral elements) representing grain boundary planes/curvatures shared between volume elements of neighboring grains. **b** Finite element meshes of variable resolution for the explicit grain structure from **a** along with C3D4, C3D10, C3D8, and C3D20 element schematics. The edge length of the cubes is taken as a unity. The total number of elements is given in Table 1

This voxel-based geometry was meshed with Cubit/Sculpt to create six initial hexahedral meshes of various mesh densities. The stair-stepped grain boundaries are smoothed by meshing (Fig. 2a). Considering both linear and quadratic element types/formulations, a total of eight meshes were created for simulations as shown in Fig. 2b. Table 1 lists the total number of elements per finite element mesh from Fig. 2b, while Table 2 and 3 shows the average number of integration points per grain and the average element edge length representing averaged element size per mesh. After selecting the microstructural cell consisting of a sufficient number of grains governing heterogeneous deformation in ST and SS,

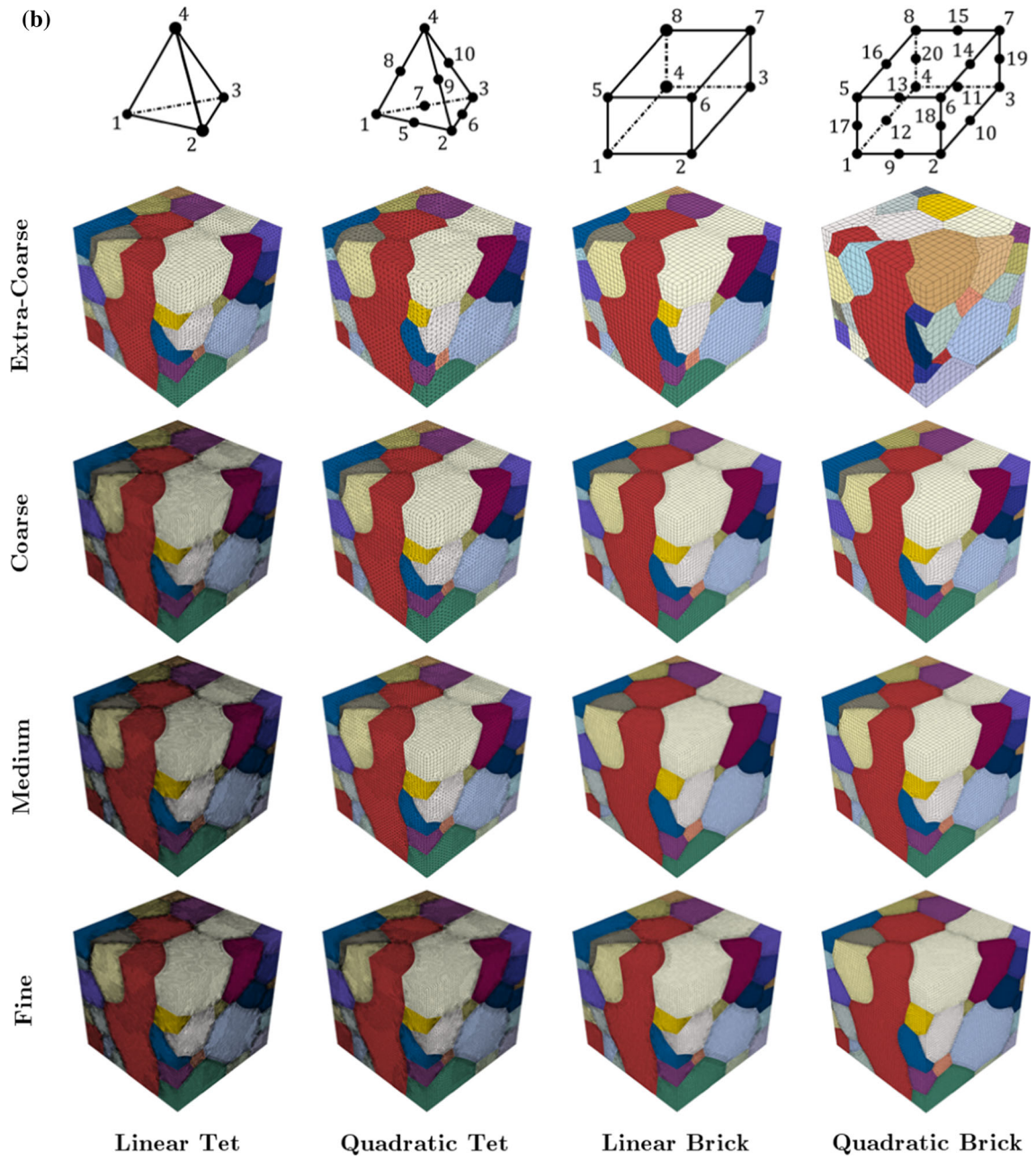

Fig. 2 continued

the grades of meshes are selected for the numerical study. These are defined based on the number of integration points and termed as fine, medium, coarse and extra-coarse. The medium grade meshes had element size similar to models used in several of our prior successful studies in which mesh sensitivity studies were performed [70, 102, 103]. The simulations were performed first with these medium grade meshes. Subsequently, coarse and fine mesh grades were created by reducing and increasing the number of integration points by a factor of approximately two. The fine grade meshes intended to further improve the accuracy of the simulations approached the limit of our computational resources, particularly in terms of the memory requirements. Four computer workstations of Intel(R) Xeon(R) Gold 6130 CPU @ 2.10 GHz with 32 physical cores and 772 GB RAM per node were recently acquired specifically for CPFE modeling and used in the present study. After performing the simulations using fine and coarse meshes, we observed that the mesh refinement slightly improved accuracy for $< 1\%$, while the mesh coarsening decreased accuracy for $< 5\%$. To decrease the accuracy more appreciably, the extra-coarse mesh grade

Table 1 Number of elements per finite element mesh from Fig. 2 categorized by an approximate number of integration points (IPs) for each mesh density (Fine, Medium, Coarse, and Extra-Coarse)

Mesh	Linear Tet (C3D4)	Quadratic Tet (C3D10)	Linear Hex (C3D8)	Quadratic Hex (C3D20)
Fine ~ 4,300,000 IPs	4,477,664	*964,865*	480,464	***215,714***
Medium ~ 2,140,000 IPs	2,651,248	559,708	***215,714***	*107,356*
Coarse ~ 900,000 IPs	*964,865*	***206,049***	*107,356*	60,058
Ex-Coarse ~ 200,000 IPs	***206,049***	57,142	24,856	10,193

The number of IPs per element type C3D4, C3D10, C3D8, and C3D20 is 1, 4, 8, and 27, respectively
Italic instances indicate the same mesh used in conjunction with two element types. Bolditalic instances indicate similar mesh density over all element types

Table 2 Average number of integration points (IPs) per grain in the explicit grain structure models

Mesh	Linear Tet	Quadratic Tet	Linear Hex	Quadratic Hex
Fine ~ 4,300,000 IPs	86,109	74,220	73,918	112,005
Medium ~ 2,140,000 IPs	50,986	43,054	33,187	55,743
Coarse ~ 900,000 IPs	18,555	15,850	16,516	31,184
Ex-Coarse ~ 200,000 IPs	3,962	4,396	3,824	5,293

Table 3 Average element edge length per mesh. Abaqus provides this distance as in between elemental nodes

Mesh	Linear Tet	Quadratic Tet	Linear Hex	Quadratic Hex
Fine	0.013413	0.009182	0.012629	0.008264
Medium	0.014774	0.012966	0.016528	0.010431
Coarse	0.018365	0.016961	0.020863	0.023644
Ex-Coarse	0.033921	0.026474	0.034753	0.032699

Considering that the quadratic elements have a node in the middle of every edge, their average edge length is split in half

was introduced by substantially reducing the number of integration points.

Pole figures showing the distribution of crystal orientations assigned to the model are shown in Fig. 1b, while "Appendix 1" lists Bunge-Euler angles and corresponding weights. There are 52 grains treated as separate element sets and each grain is randomly assigned with initially identical crystal orientation. Note that a representative volume element must have sufficient number of constituent grains to homogenize the variability arising from local microstructural features such as micro-texture, defects and phases. However, the 52 grains model used in this work is not intended to be a representative volume element but a microstructural cell facilitating the numerical study of local fields.

To create the tetrahedral meshes, a procedure described in [70] and later refined in [71] is followed. First, the surface meshes of the grains were extracted as STLs from the initial hexahedral meshes. As STLs are inherently triangular, Abaqus splits each rectangular element of the surface mesh on its diagonal to make the triangles. These STLs were then meshed in MSC Patran [104] with the internal element size coarsening enabled. Internal coarsening increases the size of the elements inside the grains, reducing the total number of elements. The total of six tetrahedral meshes with different resolutions were selected for either linear or quadratic element types. These meshes are also shown in Fig. 2b. The corresponding element counts for each mesh are shown in Table 1 along with the average number of integration points per grain and average element edge per mesh in Tables 2 and 3, respectively.

The meshes are categorized by an approximate number of IPs for each mesh density (Fine, Medium, Coarse, and Extra-Coarse). Diagonal of Table 1 (italic, bold numbers) has mesh density of approximately 200,000. Furthermore, two instances of linear and quadratic elements whether hex or tet in Table 1 have the same number of elements (italic numbers). In summary, the selected meshes of variable resolution and four element types can facilitates a variety of comparisons, which will be presented in subsequent sections of the paper. In particular, local and global mechanical fields upon deformation are compared as functions of element type and resolution of meshes i.e. degrees of freedom. Moreover, the fields are compared for a given number of integration points or a given number of elements. Finally, the simulations are compared in terms of computational time.

2.3 Boundary conditions

A simple tension boundary conditions were defined by prescribing a displacement on the top surface in the normal direction (positive Y), while ensuring the lateral surfaces to be stress-free. The simple shear case was defined similar to the simple tension case, but the prescribed displacement was along the Y-direction on the positive Z face, and the nega-

Table 4 Nodes × CPUs per node/total CPUs/total CPU time [h]/time per CPU [h] for the simple tension simulations

Mesh	Linear Tet	Quadratic Tet	Linear Hex	Quadratic Hex
Fine ~ 4,300,000 IPs	1 × 30/30/101.5/3.38	3 × 30/90/129.2/2.44	1 × 16/16/73.9/4.62	3 × 24/72/239.7/3.33
Medium ~ 2,140,000 IPs	1 × 16/16/32/2	1 × 30/30/119.8/4	1 × 30/30/17.6/0.59	1 × 30/30/76.1/2.54
Coarse ~ 900,000 IPs	1 × 16/16/5.8/0.36	1 × 30/30/12/0.4	1 × 30/30/4.5/0.15	1 × 16/16/29.8/1.86
Ex-Coarse ~ 200,000 IPs	1 × 16/16/0.8/0.05	1 × 30/30/2.0/0.07	1 × 30/30/0.7/0.02	1 × 30/30/1.4/0.05

Simulations were carried out on a workstation or multiple workstations: Intel(R) Xeon(R) Gold 6130 CPU @ 2.10 GHz with 32 physical cores and 772 GB RAM per node using various numbers of CPUs

Table 5 Nodes × CPUs per node/total CPUs/total CPU time [h]/time per CPU [h] for the simple shear simulations

Mesh	Linear Tet	Quadratic Tet	Linear Hex	Quadratic Hex
Fine ~ 4,300,000 IPs	2 × 30/60/57.3/1.0	2 × 16/32/78.6/2.5	1 × 30/30/50.0/1.7	2 × 16/32/256.6/4.0
Medium ~ 2,140,000 IPs	1 × 30/30/16.7/0.6	1 × 30/30/109.0/3.6	1 × 30/30/15.2/0.51	2 × 30/60/58.7/0.98
Coarse ~ 900,000 IPs	1 × 30/30/3.6/0.12	1 × 30/30/11.2/0.37	1 × 30/30/3.8/0.13	1 × 30/30/22.0/0.73
Ex-Coarse ~ 200,000 IPs	1 × 30/30/0.7/0.02	1 × 30/30/2.9/0.10	1 × 30/30/0.7/0.02	1 × 30/30/1.4/0.05

Simulations were carried out on a workstation or multiple workstations: Intel(R) Xeon(R) Gold 6130 CPU @ 2.10 GHz with 32 physical cores and 772 GB RAM per node using various numbers of CPUs

Table 6 Approximate memory usage in GB per simple tension simulation

Mesh	Linear Tet	Quadratic Tet	Linear Hex	Quadratic Hex
Fine ~ 4,300,000 IPs	552.9	2,508.9	266.2	1,684.9
Medium ~ 2,140,000 IPs	185.3	613.7	212.4	385.6
Coarse ~ 900,000 IPs	93.4	221.3	173.8	133.4
Ex-Coarse ~ 200,000 IPs	32.2	185.8	61.2	185.3

Table 7 Approximate memory usage in GB per simple shear simulation

Mesh	Linear Tet	Quadratic Tet	Linear Hex	Quadratic Hex
Fine ~ 4,300,000 IPs	993.6	968.9	432.2	870.1
Medium ~ 2,140,000 IPs	305.4	613.7	212.4	687.4
Coarse ~ 900,000 IPs	175.1	221.4	173.7	216.4
Ex-Coarse ~ 200,000 IPs	173.7	185.3	61.2	185.3

tive Z face was constrained in the Y direction. Prescribed displacement was $U = 0.22$ for both tension and shear at approximate strain rate of 0.001/s and at room temperature. (Note that the polycrystalline domain has a size of 1). In all simulations, direct sparse solver in Abaqus was used and the initial time step was 0.0001 s, the maximum and the minimum time steps of 4 s and 0.00002 s were assigned, respectively.

3 Simulation results

A CPFE model coupled with the implicit finite element software Abaqus/Standard is used to solve the boundary value problem corresponding to simple tension (ST) and simple shear (SS) of the microstructural cell. A total of 32 simulations have been performed and post-processed for this paper. The simulations performed were demanding in both RAM size requirement as well as computational time. Computational time required to complete the jobs is presented in Tables 4 and 5 given the number of elements and their degrees-of-freedom and the boundary conditions. As is indicated in the table, the MPI parallel computing infrastructure available in Abaqus was utilized. Given the CPFE model storing variables pertaining to the crystallography such as crystal orientations, Schmid tensors etc. in addition to stress–strain measures and underlying state variables pertaining to the hardening law such as slip resistance and dislocation densities, Table 6, 7 shows the memory requirement per simulation. Note that the memory usage is a function of the number of used CPUs per simulation (Tables 4, 5).

Figures 3 and 4 show von Mises stress, while "Appendix 2" presents equivalent strain and pressure contours after ST and SS to a displacement of $U = 0.22$. Minor sensitivity of models to the boundary conditions ST vs SS can be observed. Qualitative comparison reveals that the models predict strong/hot versus weak/cold spots in the microstructure independent on the level of discretization. Nevertheless, the predicted

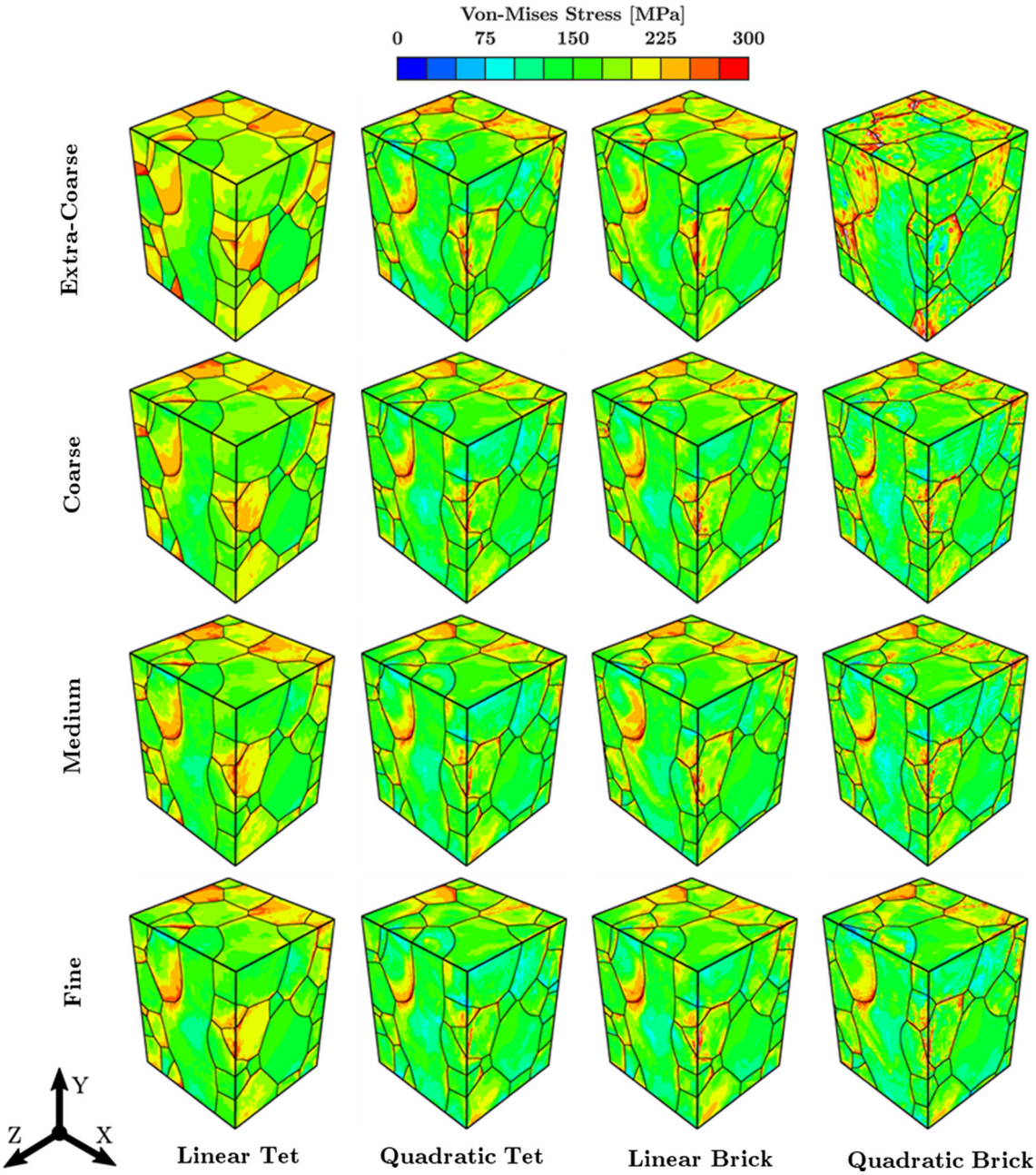

Fig. 3 Von Mises stress contours after simple tension to a displacement of $U = 0.22$

contours are different for most of the models with the extra-coarse models exhibiting the obvious deviations.

Further consideration of the fields as a function of element type shows that the discontinuities in the fields and the largest heterogeneities are present in the quadratic hexahedral extra-coarse model. Large deviations are also present across the linear tet models. Interestingly the largest range of values in pressure as well as heterogeneity in pressure fields exhibits the extra coarse quadratic hexahedra mesh. The fields become smoother with mesh resolution but still hot/cold spots are present. Linear tetrahedral element also exhibits a large range of values in pressure. Fields predicted by quadratic tetrahedral and linear hexahedral appear to be similar, especially for medium and fine mesh resolutions.

To further investigate internal fields, Fig. 5 shows contours over the surface for a central grain. Figure 6 compares models quantitatively, in terms of stress versus strain components for the central grain using stress–strain curves and a suitably defined error measure at the middle and at the end of deformation for both ST and SS. While the overall trends in the stress–strain curves are similar, the linear tet elements

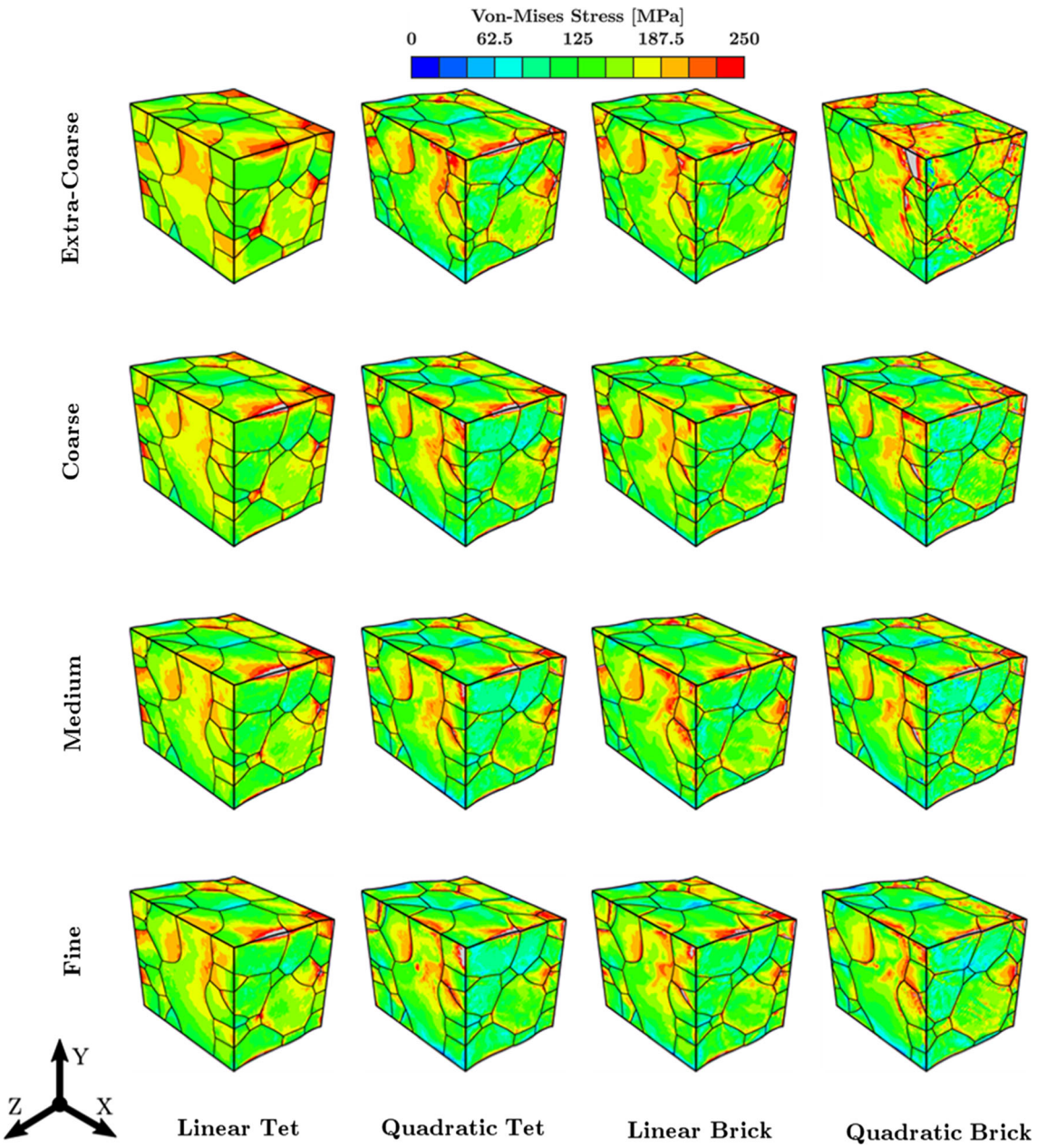

Fig. 4 Von Mises stress contours after simple shear to a displacement of 0.22

deviate from the predictions using the other element types. The error is defined as

$$\%Error(mesh_i) = \frac{\left|\int_V \sigma_{ij}(mesh_i) - \int_V \sigma_{ij}(QTet_{964865})\right|}{\int_V \sigma_{ij}(QTet_{964865})}, \tag{15}$$

where V is the volume of central grain, while $\sigma_{ij} = \sigma_{22}$ is for ST and $\sigma_{ij} = \sigma_{23}$ is for SS. The error is relative to the fine Qtet-964,865 model (Fig. 2b). As is evident, the quantitative comparisons reveal that linear tet elements introduce a large error in CPFE calculations, even with substantially increased mesh resolution. Interestingly the linear brick elements develop the smallest rate of deviation in the fields with mesh coarsening amongst the studied element types. In contrast, the quadratic brick elements develop the greatest amount of deviation with mesh coarsening. The use of extra-coarse meshes leads to inaccuracy, as expected independent on the element type. While the figure quantifies errors as a function of the simulation method for the central grain only, similar trends are predicted for any other individual grain or a group of grains or the overall model. Importantly, predictions of grain averaged stresses as calculated here can be validated

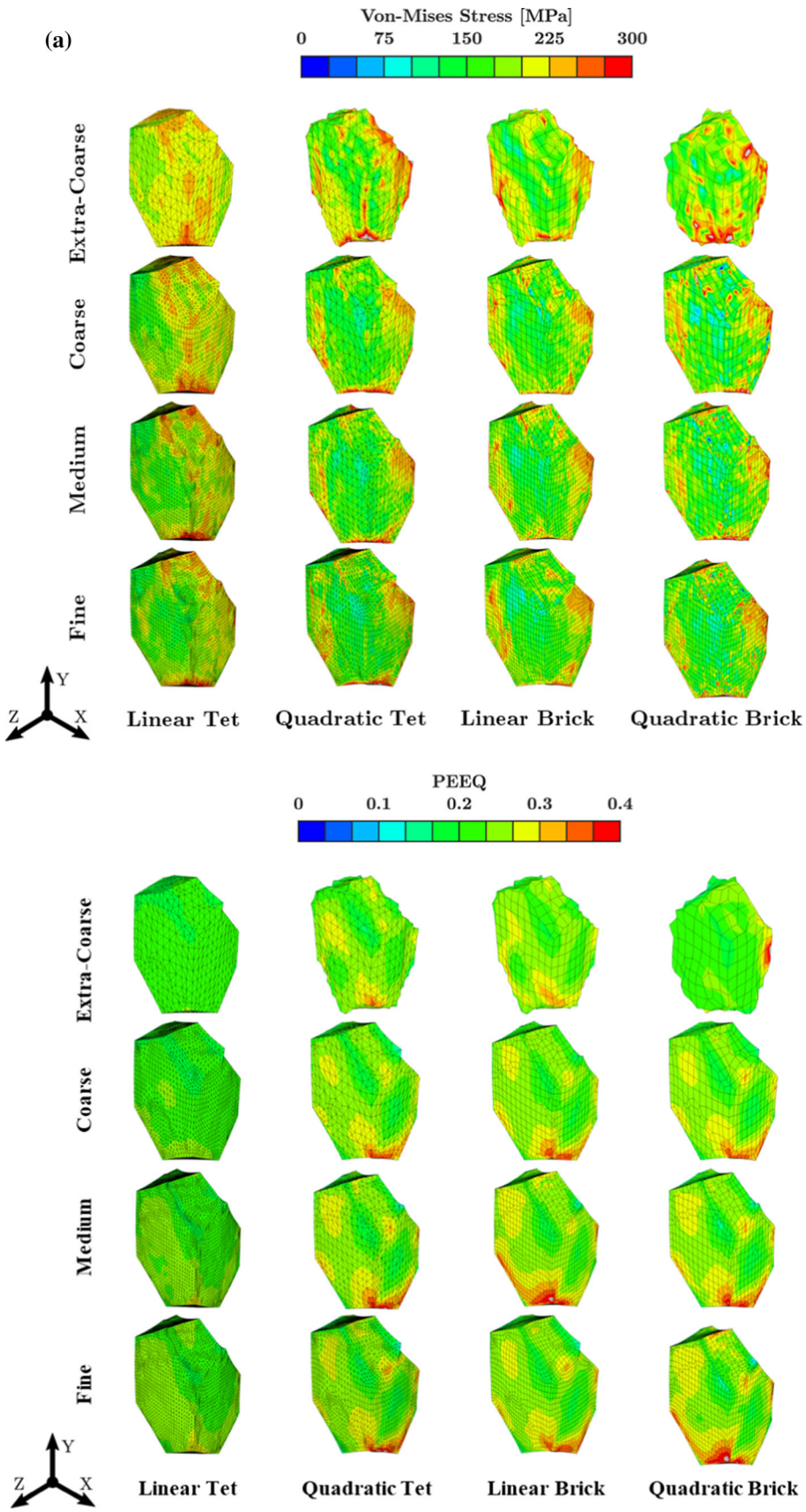

Fig. 5 Contours of selected mechanical fields for the central grain deformed in **a** ST and **b** SS

Fig. 5 continued

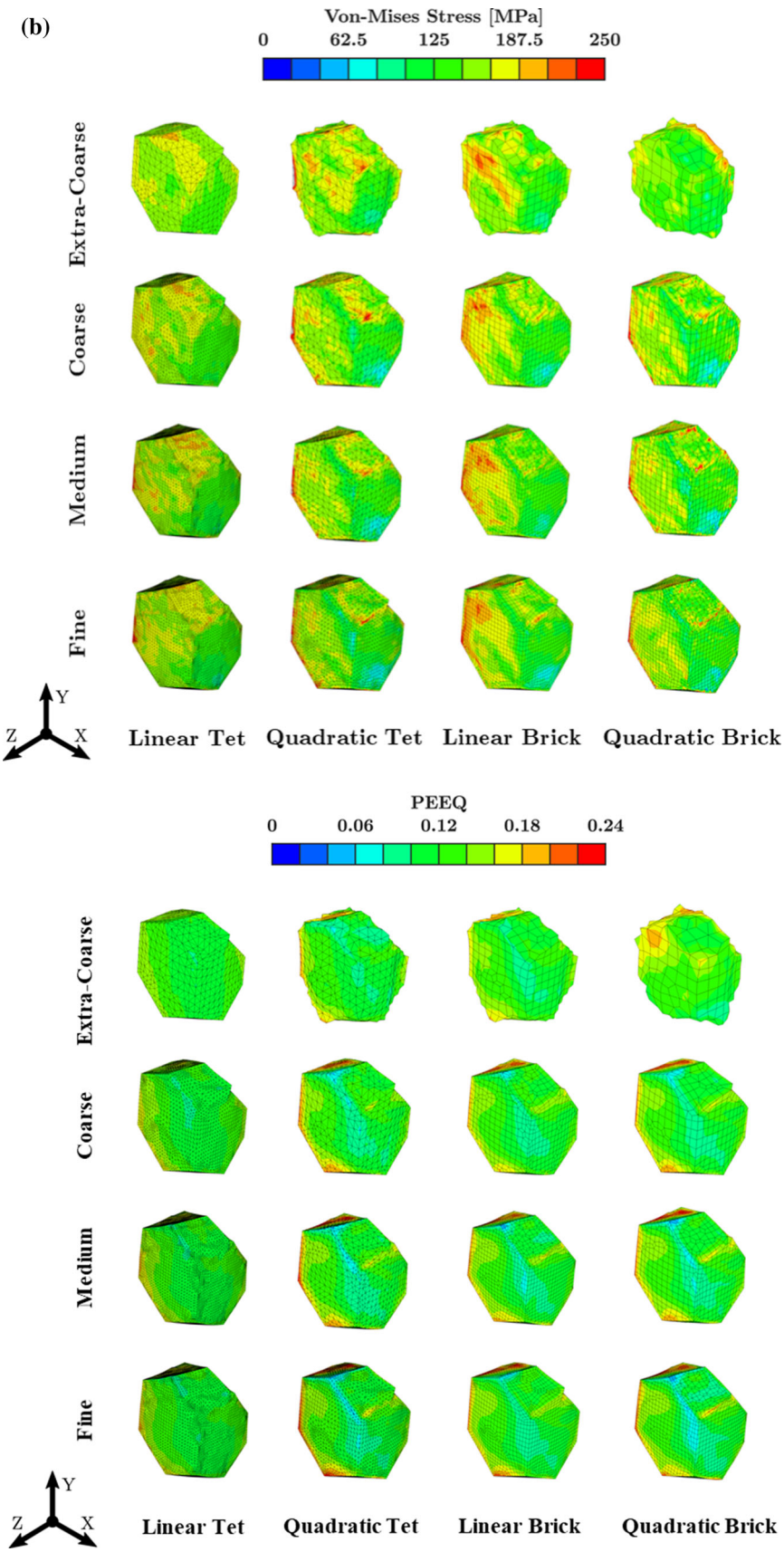

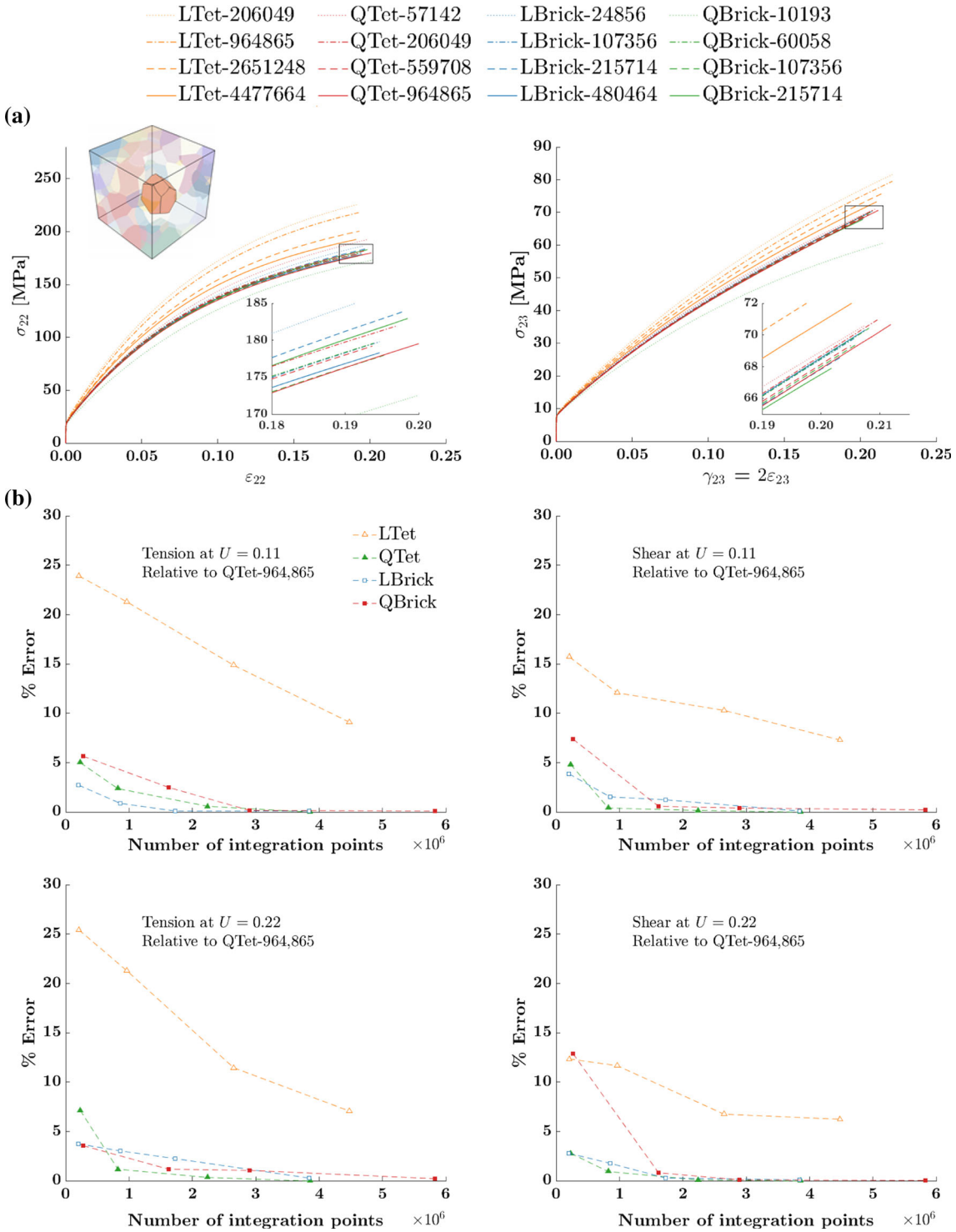

Fig. 6 **a** Stress component—strain component curves for the central grain. The insert shows the location of the central grain. **b** Error plots defined using Eq. (15) after the displacement of $U = 0.11$ and $U = 0.22$

using high energy synchrotron x-rays. The methodology is being used to measure such grain averaged quantities.

4 Discussion

This work presents results from 32 large-scale simulations with four element types at various mesh resolutions to under-

stand discretization errors in polycrystalline CPFE models. To authors knowledge, this is the first study comparing quantitatively the solution accuracy and computational time as a function of element type and mesh resolution in CPFE simulations of polycrystalline grain structures. The starting model is a voxel-based polycrystalline grain structure (microstructural cell) created synthetically by a phase field grain growth simulation, which is then converted to interface conformal hexahedral and tetrahedral meshes. In doing so, procedures for interface-conformal mesh generation over complex shapes for tetrahedral and hexahedral elements are advanced. The procedures rely on software packages Patran and Cubit/Sculpt, respectively. Note that while interface conformal FE meshes are preferred, especially for predicting localized behavior such as damage formation and failure, it is very challenging to rapidly generate 3D conformal meshes of polycrystalline microstructures. The inherent difficulties in describing complex shapes with hexahedral elements as opposed to relatively flexible tetrahedral elements make the latest version of Cubit/Sculpt very successful mesh generation tool to obtain interface-conformal hexahedral meshes of polycrystalline microstructures. Also note that the time to generate hexahedral mesh is significantly longer and is semi-automatic, mainly due to additional operations (inclusion of elements and smoothing) to maintain good mesh quality, relative to automatic and rapid mesh generation of tetrahedral mesh starting from the surface mesh of constituent grains.

Given the element type and the number of elements i.e. their degrees-of-freedom, the computational time involved in simulations varied. A parallel computing infrastructure is utilized to run the jobs on a single or multiple workstations working concurrently. CPFE simulations with various finite element meshes show the trend that the computational time per CPU scales with the degrees of freedom for every element type. As expected, models with more elements require more time per CPU than smaller sized models. As the time per CPU scales with the number of degrees of freedom, linear elements are faster per CPU than the corresponding quadratic elements. Since brick elements show faster convergence rate than tetrahedral elements, even the linear brick elements approach at an equivalent solution accuracy at cheaper computational cost relative to the quadratic tetrahedral elements.

The study of element type and mesh resolution is essential for attempting to predict the evolutions of local fields during plastic deformation, i.e. local stress–strain developments, especially while predicting phenomena such as void formations and propagation. Such studies are challenging in crystal plasticity modeling as these models are not only computationally intensive but also rely on explicit meshing of grain structure using a large number of elements of an appropriate type. Resolving every grain within a grain structure domain complicates mesh convergence study as the convergence is strongly influenced by the initial shape and size of grains, crystallography, global and local loadings as a consequence of applied boundary conditions and also the hardening law to a smaller extent. Figure 7 shows locations of the peak stress localizations upon ST and SS simulations performed in the present work. As is evident, the 'hot spot' is at a triple junction for the model deformed in ST and at a grain boundary for the model deformed in SS. The actual location is therefore dependent on the imposed boundary condition and also varies with the element type and mesh refinement. Specifically, while linear/quadratic hex and quadratic tet consistently predict the same locations of the hot spots in stress, the liner tet elements deviate and vary with mesh resolution. Additionally, quadratic hex elements over predict the level of pressure and resulting stress triaxiality. As a result, these elements are not recommended for studying voiding in polycrystals.

Simulation results in this work suggest that linear tetrahedral element is not appropriate for CPFE modeling of grain structures, although a number of studies utilized it in grain structure modeling, including the works of present authors [70, 72]. These elements are overly stiff requiring extremely fine meshes to arrive at accurate solutions [105]. Moreover, these elements are susceptible to volumetric locking in modeling of incompressible solids (pressure plots in Figs. 3 and 4). Mesh refinement to about 4.5×10^6 linear tetrahedral elements requires large RAM memory. Such refinement only reduced the error to about 10% (Fig. 6). Further refinement becomes impractical because of enormous CPU memory and # of cores requirements. Key advantages of tetrahedral elements are their geometric adaptability and suitability for rapid and automatic meshing algorithms. These elements are very convenient to discretize complex shapes. However, it is possible to take these advantages only for quadratic tetrahedral elements, as will be discussed shortly.

The discussion above has focused primarily on the performances of linear tetrahedral elements for modeling of grain structures. We now focus on the performances of the hexahedral elements. Quadratic hexahedral elements are not recommended for severe element distortions as a consequence of large plastic strains or very high strain gradients [105]. According to the Abaqus User Manual [105], second-order reduced-integration elements in Abaqus/Standard are likely to be more accurate than the corresponding fully-integrated elements. Considering that C3D20 has 27 IPs, while the corresponding C3D20R reduced integration element has only 8 IPs, the simulations are faster by approximately a factor of three. However, these simulations are not performed in the present work because the linear brick elements and C3D20R yield similar results. For the first-order reduced integration (C3D8R) hexahedral element is not recommended primarily due to its propensity to the hourglass effect [105]. In contrast, while the fully integrated elements do not show the hourglass effect, they are susceptible to volumetric locking. As stated above, the volumetric locking can appear for fully

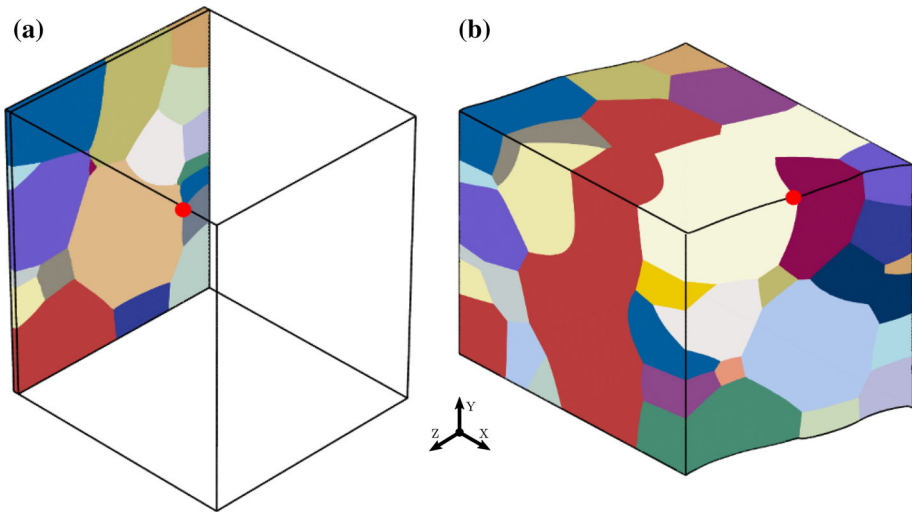

Fig. 7 Locations of the mechanical extremes per model indicated by red dots after (a) ST and (b) SS

integrated elements while modeling incompressible solids. Spurious pressure fields can arise at IPs, causing the element to behave as very stiffly while enforcing the volume conservation. Quadratic fully integrated elements are the most susceptible to lock at larger plastic strains. However, the reduced-integration of quadratic elements eliminates volumetric locking. In contrast to quadratic elements, linear hexahedral elements selectively use reduced integration and do not lock. Mesh refinement helps to reduce volumetric locking of quadratic elements. Pressure fields in Figs. 3 and 4 show a checkerboard pattern, especially for quadratic hexahedral elements. The checkerboard pattern is a sign of volumetric locking. As is evident, mesh refinement helps in reducing the pattern. Moreover, quadratic hexahedral elements are the element type first to introduce error greater than 5% relative to the fine Qtet-964,865 mesh with coarsening the resolution for a given number of integration points. The error comes at the expense of losing some geometry features with coarsening hexahedral elements.

Our results suggest that quadratic tetrahedral and linear hexahedral elements are recommended for CPFE modeling of grain structures. According to the pressure maps, linear hexahedral elements are least prone to volumetric locking. Also, hexahedral elements usually converged to a solution of equivalent accuracy at less computational cost compared to quadratic tetrahedral elements. Considering that shape of the grains is very complex and far from being rectangular for hexahedral elements, tetrahedral elements are far more flexible and desirable. Therefore, although structured hexahedral elements in 3D analyses are desirable, since they give the best results with the minimum computational cost, tetrahedral elements are recommended. Extra coarse tetrahedral elements still describe the geometry reasonably well while hexahedral elements fail to capture the geometry (Fig. 2b).

Excluding linear tetrahedral elements, CPFE simulations show that the deviation between model predictions with about 200,000 elements performed using different element types would be within 5%. Further mesh refinements improve the accuracy at the expense of increasing the computational time and memory requirements. This strongly suggests that quadratic tetrahedral elements are the best compromise between accuracy and computational speed in CPFE simulation of polycrystals.

5 Conclusions

Suitability of the four most commonly used element types along with varying mesh resolution in CPFE modeling of grain structures are investigated using large-scale simulations. A voxel-based polycrystalline grain structure is generated by a phase field grain growth simulation and converted to interface conformal hexahedral and tetrahedral element meshes of variable resolution. Procedures for such interface-conformal mesh generation over complex shapes relying on Patran for tetrahedral and Cubit/Sculpt for hexahedral elements are described. CPFE simulations of simple tension and simple shear deformation conditions are performed. Minor sensitivity of models to these boundary conditions is observed. The computational time per CPU was measured to scale with the degrees of freedom for every element type. As the time per CPU scales with the number of degrees of freedom, linear elements are faster per CPU than the corresponding quadratic elements. However, hexahedral elements exhibit a better convergence rate than quadratic tetrahedral elements and arrive at a solution of equivalent accuracy to quadratic tetrahedral elements at less computational cost. Simulation results suggest that linear tetrahedral element is not appropriate for CPFE modeling of grain structures as these elements are overly stiff. Mesh refinement only moderately improve such simulation results. Results also show that quadratic brick elements are not suitable for

large plastic straining of complex geometries due to their propensity to volumetric locking. Similarly, mesh refinement only reduces the checkerboard pattern in pressure fields. The mesh resolution studies in capturing mechanical fields shows that brick elements are more sensitive than tetrahedral elements, which can be associated to geometric adaptability of tetrahedral elements. Geometry features can be lost with brick element coarsening. Moreover, tetrahedral elements are suitability for rapid and automatic meshing algorithms. In summary, quadratic tetrahedral and linear hexahedral elements are more accurate for crystal plasticity finite element modeling than linear tetrahedral and quadratic hexahedral elements. Furthermore, tetrahedral elements are more desirable due to fast mesh generation and flexibility to describe complex grain structure geometries. It is anticipated that the results from this study provide useful guidance for future CPFE modeling of grain structures. These guidance should be applicable to other crystal plasticity models as constitutive models and hardening formulations have minor effects on mesh sensitivity.

Acknowledgements This work is based upon a project supported by the U.S. National Science Foundation under grant no. CMMI-1650641. The authors gratefully acknowledge this support. This paper describes objective technical results and analysis. Any subjective views or opinions that might be expressed in the paper do not necessarily represent the views of the U.S. Department of Energy or the United States Government. Sandia National Laboratories is a multi-mission laboratory managed and operated by National Technology and Engineering Solutions of Sandia, LLC., a wholly owned subsidiary of Honeywell International, Inc., for the U.S. Department of Energy's National Nuclear Security Administration under contract DE-NA0003525.

Appendix 1

See Table 8.

Table 8 Bunge-Euler angles (ϕ_1, Φ, ϕ_2) in degrees and corresponding volume fraction (VF) of crystals used to initialize the model

#	ϕ_1	Φ	ϕ_2	VF	#	ϕ_1	Φ	ϕ_2	VF
1	285.4	78.7	30.5	0.005631	27	285.4	78.2	21.5	0.024535
2	39.5	60.7	12.8	0.070512	28	351.2	62.8	30.5	0.003533
3	338	86.1	21.5	0.155554	29	188.8	50.7	12.8	0.000113
4	250.2	50.7	12.8	0.012342	30	127.3	86.1	21.5	0.038058
5	144.9	86.1	21.5	0.001854	31	4.4	77.7	4.3	0.012009
6	153.7	61.5	21.5	0.087928	32	22	64.8	40.1	0.00757
7	180	78.7	30.5	0.061393	33	57.1	78.2	21.5	0.063121
8	285.4	53.3	30.5	0.012954	34	22	51.7	21.5	0.024633
9	188.8	86.1	21.5	0.000647	35	232.7	60.7	12.8	0.011798
10	180	86	12.8	0.031774	36	285.4	50.3	4.3	0.003005
11	294.1	60.7	12.8	0.000082	37	223.9	51.7	21.5	0.001046
12	232.7	64.8	40.1	0.009366	38	118.5	72.3	40.1	0.041698
13	65.9	86.2	30.5	0.004408	39	259	70.1	21.5	0.004197
14	136.1	77.7	4.3	0.001502	40	48.3	86.5	40.1	0.001065
15	162.4	53.3	30.5	0.000314	41	250.2	86.1	21.5	0.001816
16	338	50.7	12.8	0.021943	42	101	77.9	12.8	0.000527
17	294.1	50.3	4.3	0.036506	43	223.9	86.2	30.5	0.003741
18	144.9	77.9	12.8	0.025753	44	30.7	62.8	30.5	0.002037
19	92.2	79.5	40.1	0.000605	45	22	86	12.8	0.001655
20	351.2	64.8	40.1	0.002333	46	109.8	50.7	12.8	0.001142
21	144.9	78.2	21.5	0.000108	47	320.5	85.9	4.3	0.025865
22	13.2	78.2	21.5	0.026761	48	30.7	86	12.8	0.010391
23	48.3	62.8	30.5	0.006717	49	22	69.3	4.3	0.03423
24	171.2	72.3	40.1	0.010872	50	329.3	78.2	21.5	0.04146
25	241.5	60.7	12.8	0.000311	51	57.1	86.2	30.5	0.01531
26	153.7	60.7	12.8	0.027493	52	136.1	86.5	40.1	0.009783

Appendix 2

See Figs. 8 and 9.

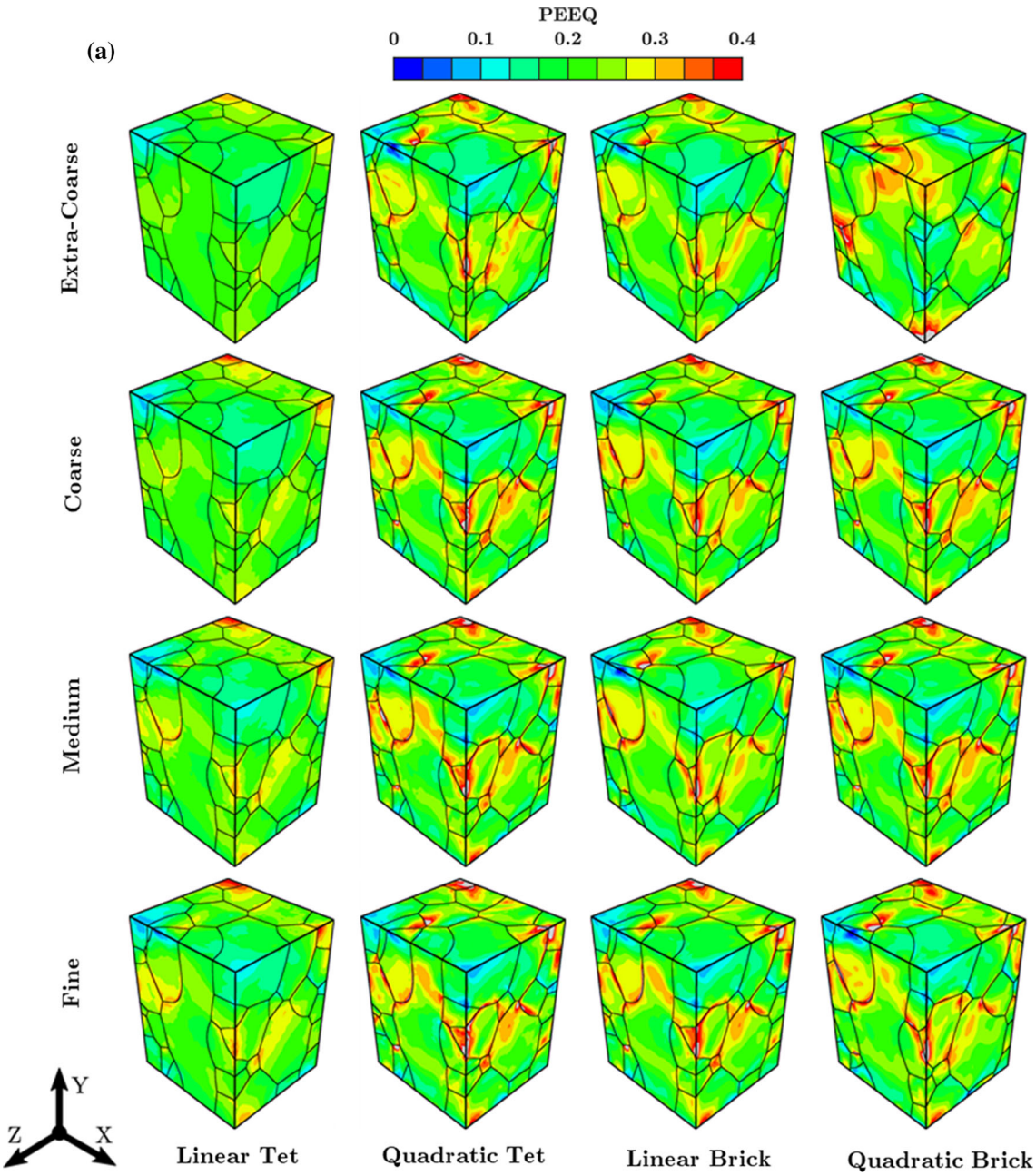

Fig. 8 **a** Equivalent strain and **b** pressure contours after simple tension to a displacement of $U = 0.22$

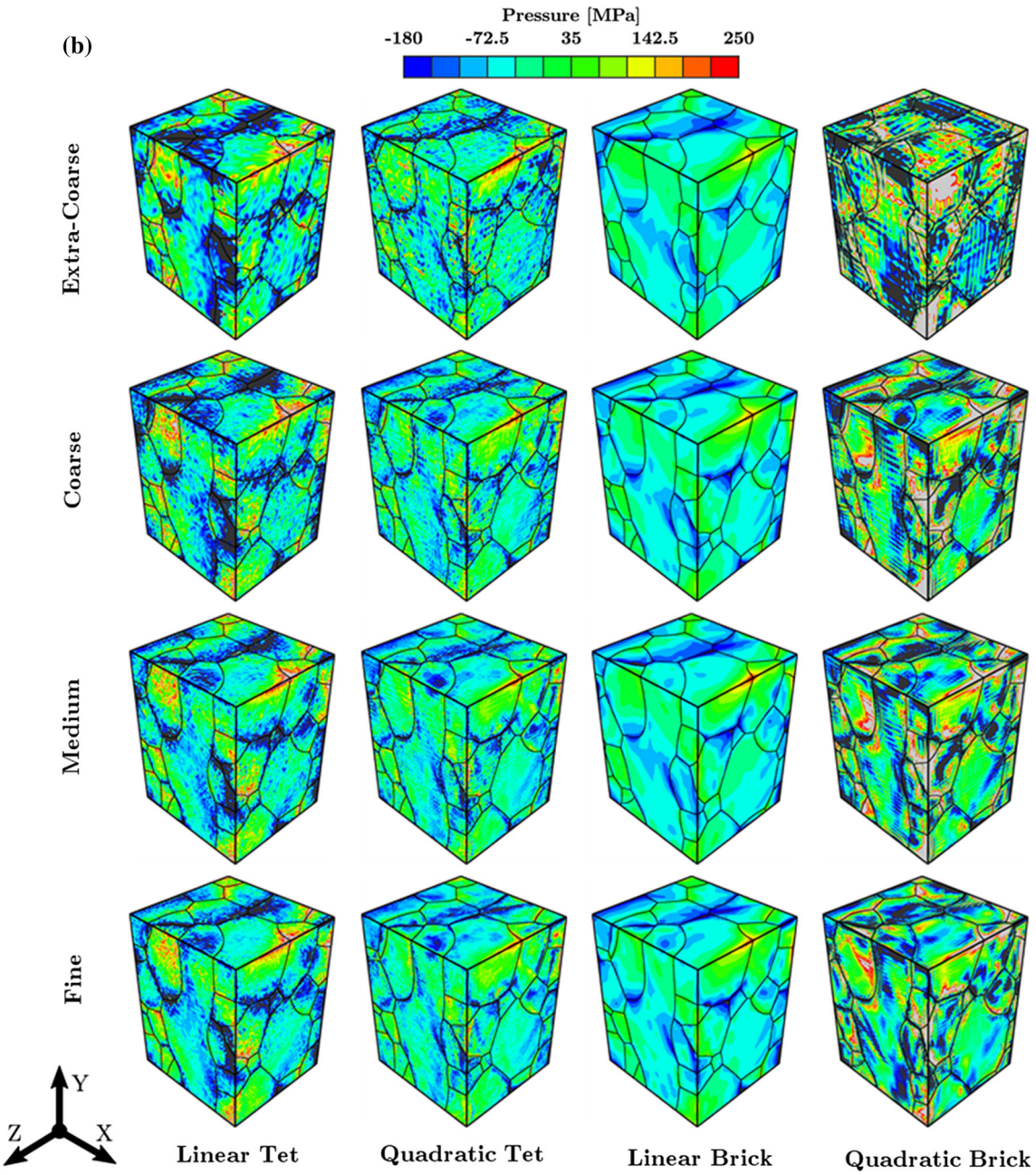

Fig. 8 continued

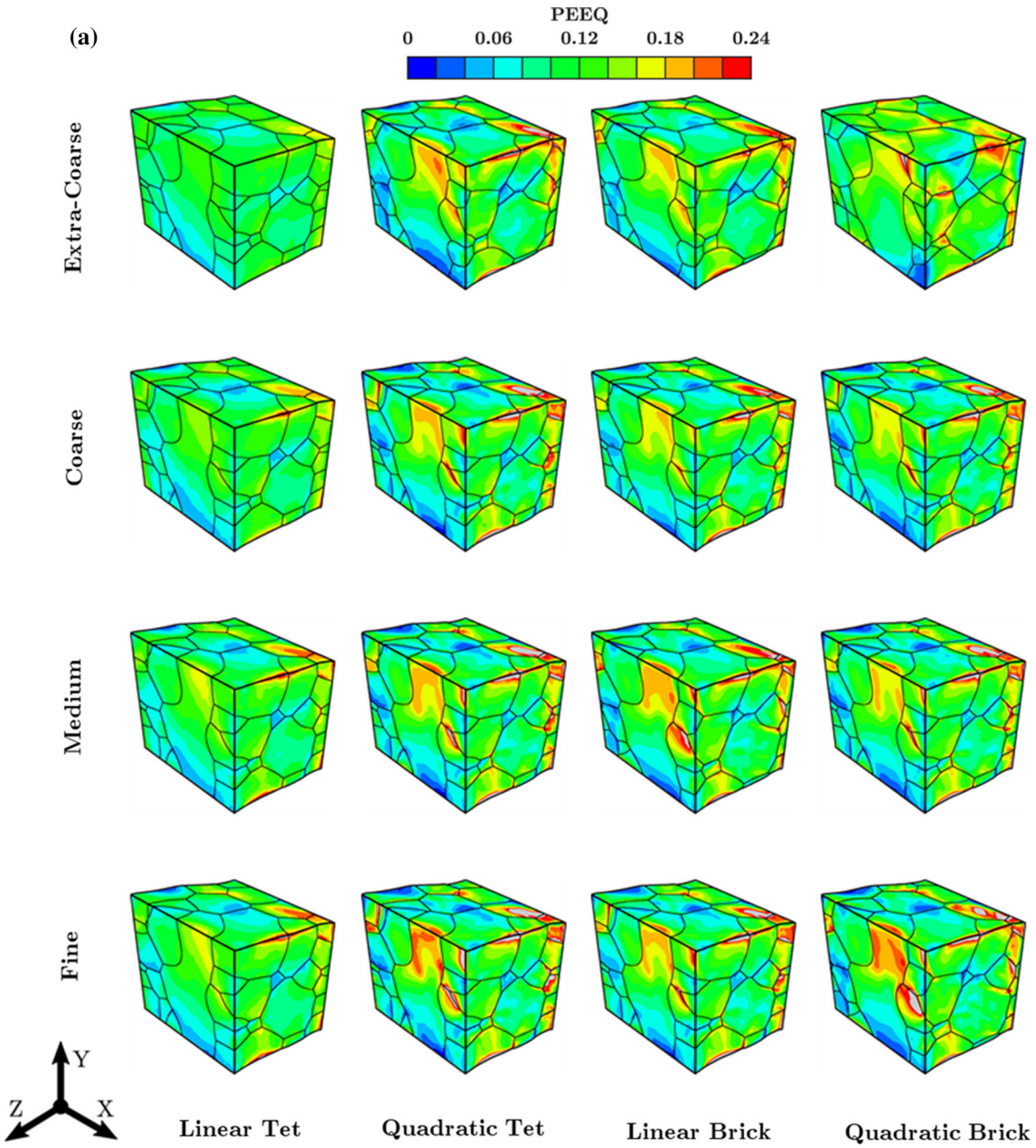

Fig. 9 **a** Equivalent strain and **b** pressure contours after simple shear to a displacement of 0.22

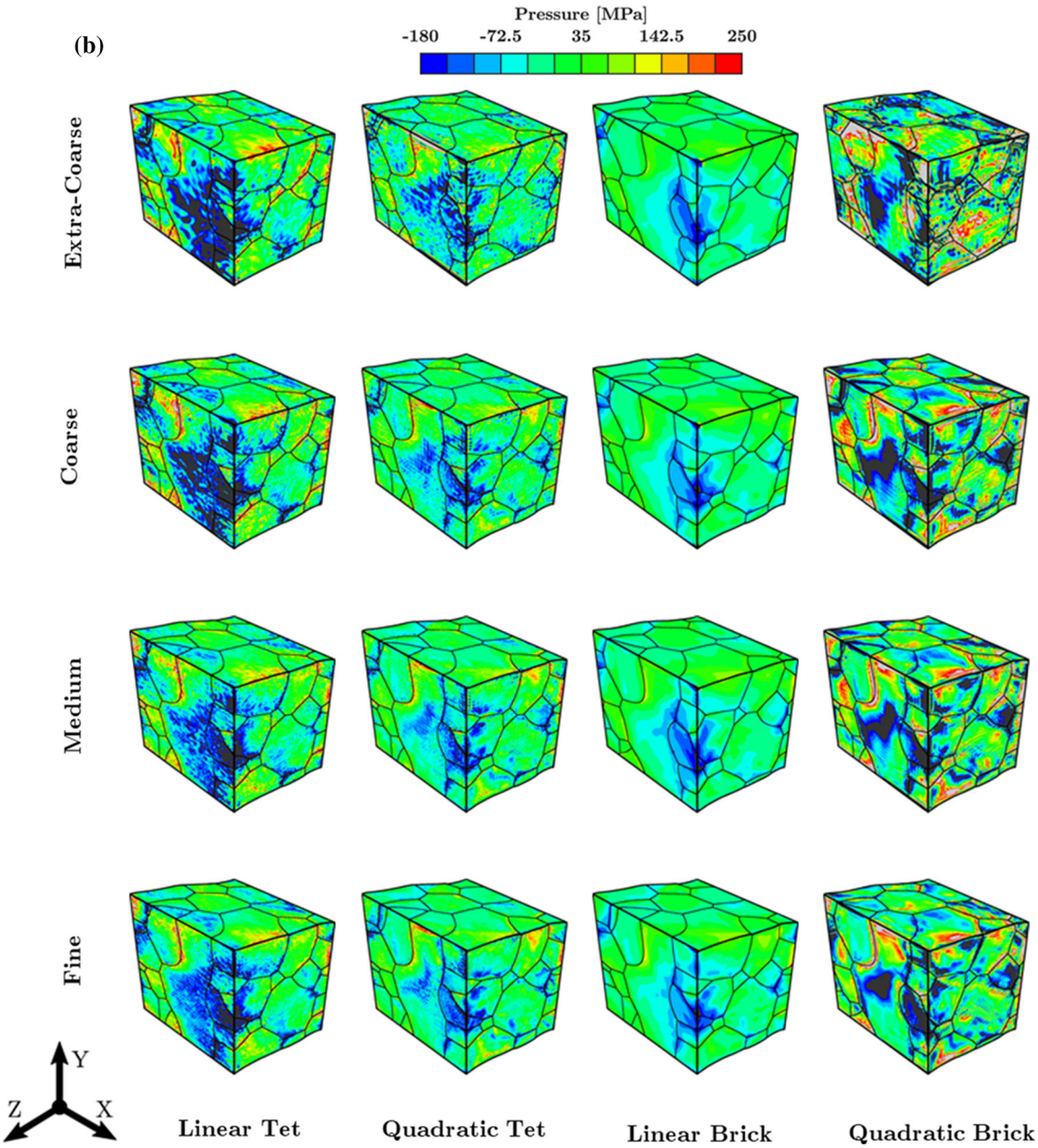

Fig. 9 continued

References

1. Eghtesad A, Zecevic M, Lebensohn RA, McCabe RJ, Knezevic M (2018) Spectral database constitutive representation within a spectral micromechanical solver for computationally efficient polycrystal plasticity modelling. Comput Mech 61:89–104
2. Bathe K-J (1996) Finite element procedures. Englewood Cliffs, Prentice Hall
3. Eghtesad A, Barrett TJ, Germaschewski K, Lebensohn RA, McCabe RJ, Knezevic M (2018) OpenMP and MPI implementations of an elasto-viscoplastic fast Fourier transform-based micromechanical solver for fast crystal plasticity modeling. Adv Eng Softw 126:46–60
4. Eghtesad A, Germaschewski K, Lebensohn RA, Knezevic M (2020) A multi-GPU implementation of a full-field crystal plasticity solver for efficient modeling of high-resolution microstructures. Comput Phys Commun 1:107231
5. Peirce D, Asaro RJ, Needleman A (1982) An analysis of nonuniform and localized deformation in ductile single crystals. Acta Metall 30:1087–1119
6. Diard O, Leclercq S, Rousselier G, Cailletaud G (2002) Distribution of normal stress at grain boundaries in multicrystals: application to an intergranular damage modeling. Comput Mater Sci 25:73–84
7. Jahedi M, Ardeljan M, Beyerlein IJ, Paydar MH, Knezevic M (2015) Enhancement of orientation gradients during simple shear

deformation by application of simple compression. J Appl Phys 117:214309
8. Ardeljan M, McCabe RJ, Beyerlein IJ, Knezevic M (2015) Explicit incorporation of deformation twins into crystal plasticity finite element models. Comput Methods Appl Mech Eng 295:396–413
9. Zhao Z, Ramesh M, Raabe D, Cuitiño AM, Radovitzky R (2008) Investigation of three-dimensional aspects of grain-scale plastic surface deformation of an aluminum oligocrystal. Int J Plast 24:2278–2297
10. Lim H, Carroll JD, Battaile CC, Buchheit TE, Boyce BL, Weinberger CR (2014) Grain-scale experimental validation of crystal plasticity finite element simulations of tantalum oligocrystals. Int J Plast 60:1–18
11. Savage DJ, Beyerlein IJ, Knezevic M (2017) Coupled texture and non-Schmid effects on yield surfaces of body-centered cubic polycrystals predicted by a crystal plasticity finite element approach. Int J Solids Struct 109:22–32
12. Knezevic M, Levinson A, Harris R, Mishra RK, Doherty RD, Kalidindi SR (2010) Deformation twinning in AZ31: influence on strain hardening and texture evolution. Acta Mater 58:6230–6242
13. Kalidindi SR, Bronkhorst CA, Anand L (1992) Crystallographic texture evolution in bulk deformation processing of FCC metals. J Mech Phys Solids 40:537–569
14. Kalidindi SR, Duvvuru HK, Knezevic M (2006) Spectral calibration of crystal plasticity models. Acta Mater 54:1795–1804
15. Miehe C, Schröder J, Schotte J (1999) Computational homogenization analysis in finite plasticity Simulation of texture development in polycrystalline materials. Comput Methods Appl Mech Eng 171:387–418
16. Beaudoin AJ, Dawson PR, Mathur KK, Kocks UF, Korzekwa DA (1994) Application of polycrystal plasticity to sheet forming. Comput Methods Appl Mech Eng 117:49–70
17. Sarma GB, Dawson PR (1996) Texture predictions using a polycrystal plasticity model incorporating neighbor interactions. Int J Plast 12:1023–1054
18. Ardeljan M, Beyerlein IJ, Knezevic M (2014) A dislocation density based crystal plasticity finite element model: application to a two-phase polycrystalline HCP/BCC composites. J Mech Phys Solids 66:16–31
19. Sarma GB, Dawson PR (1996) Effects of interactions among crystals on the inhomogeneous deformations of polycrystals. Acta Mater 44:1937–1953
20. Mika DP, Dawson PR (1998) Effects of grain interaction on deformation in polycrystals. Mater Sci Eng A 257:62–76
21. Delannay L, Jacques PJ, Kalidindi SR (2006) Finite element modeling of crystal plasticity with grains shaped as truncated octahedrons. Int J Plast 22:1879–1898
22. Ritz H, Dawson P (2008) Sensitivity to grain discretization of the simulated crystal stress distributions in FCC polycrystals. Modell Simul Mater Sci Eng 17:015001
23. Kalidindi SR, Bhattacharya A, Doherty R (2004) Detailed Analysis of Plastic Deformation in Columnar Polycrystalline Aluminum Using Orientation Image Mapping and Crystal Plasticity Models. Proc R Soc Lond Math Phys Eng Sci 460:1935–1956
24. Diard O, Leclercq S, Rousselier G, Cailletaud G (2005) Evaluation of finite element based analysis of 3D multicrystalline aggregates plasticity: application to crystal plasticity model identification and the study of stress and strain fields near grain boundaries. Int J Plast 21:691–722
25. Shenoy M, Tjiptowidjojo Y, McDowell D (2008) Microstructure-sensitive modeling of polycrystalline IN 100. Int J Plast 24:1694–1730
26. Ardeljan M, Savage DJ, Kumar A, Beyerlein IJ, Knezevic M (2016) The plasticity of highly oriented nano-layered Zr/Nb composites. Acta Mater 115:189–203
27. Lim H, Battaile CC, Bishop JE, Foulk JW (2019) Investigating mesh sensitivity and polycrystalline RVEs in crystal plasticity finite element simulations. Int J Plast 121:101–115
28. Lim H, Abdeljawad F, Owen SJ, Hanks BW, Foulk JW, Battaile CC (2016) Incorporating physically-based microstructures in materials modeling: bridging phase field and crystal plasticity frameworks. Modell Simul Mater Sci Eng 24:045016
29. Lim H, Carroll JD, Battaile CC, Boyce BL, Weinberger CR (2015) Quantitative comparison between experimental measurements and CP-FEM predictions of plastic deformation in a tantalum oligocrystal. Int J Mech Sci 92:98–108
30. Knezevic M, Kalidindi SR (2007) Fast computation of first-order elastic-plastic closures for polycrystalline cubic-orthorhombic microstructures. Comput Mater Sci 39:643–648
31. Taylor GI (1938) Plastic strain in metals. J Inst Met 62:307–324
32. Lebensohn RA, Tomé CN (1993) A self-consistent anisotropic approach for the simulation of plastic deformation and texture development of polycrystals: application to zirconium alloys. Acta Metall Mater 41:2611–2624
33. Lebensohn RA, Zecevic M, Knezevic M, McCabe RJ (2016) Average intragranular misorientation trends in polycrystalline materials predicted by a viscoplastic self-consistent approach. Acta Mater 104:228–236
34. Zecevic M, Pantleon W, Lebensohn RA, McCabe RJ, Knezevic M (2017) Predicting intragranular misorientation distributions in polycrystalline metals using the viscoplastic self-consistent formulation. Acta Mater 140:398–410
35. Knezevic M, Kalidindi SR, Fullwood D (2008) Computationally efficient database and spectral interpolation for fully plastic Taylor-type crystal plasticity calculations of face-centered cubic polycrystals. Int J Plast 24:1264–1276
36. Knezevic M, Al-Harbi HF, Kalidindi SR (2009) Crystal plasticity simulations using discrete Fourier transforms. Acta Mater 57:1777–1784
37. Zecevic M, Knezevic M, Beyerlein IJ, McCabe RJ (2016) Origin of texture development in orthorhombic uranium. Mater Sci Eng A 665:108–124
38. Knezevic M, Beyerlein IJ, Lovato ML, Tomé CN, Richards AW, McCabe RJ (2014) A strain-rate and temperature dependent constitutive model for BCC metals incorporating non-Schmid effects: application to tantalum–tungsten alloys. Int J Plast 62:93–104
39. Knezevic M, Capolungo L, Tomé CN, Lebensohn RA, Alexander DJ, Mihaila B, McCabe RJ (2012) Anisotropic stress-strain response and microstructure evolution of textured α-uranium. Acta Mater 60:702–715
40. Knezevic M, Nizolek T, Ardeljan M, Beyerlein IJ, Mara NA, Pollock TM (2014) Texture evolution in two-phase Zr/Nb lamellar composites during accumulative roll bonding. Int J Plast 57:16–28
41. Knezevic M, Savage DJ (2014) A high-performance computational framework for fast crystal plasticity simulations. Comput Mater Sci 83:101–106
42. Knezevic M, Zecevic M, Beyerlein IJ, Lebensohn RA (2016) A numerical procedure enabling accurate descriptions of strain rate-sensitive flow of polycrystals within crystal visco-plasticity theory. Comput Methods Appl Mech Eng 308:468–482
43. Savage DJ, Knezevic M (2015) Computer implementations of iterative and non-iterative crystal plasticity solvers on high performance graphics hardware. Comput Mech 56:677–690
44. Barrett TJ, Knezevic M (2019) Deep drawing simulations using the finite element method embedding a multi-level crystal plasticity constitutive law: experimental verification and sensitivity analysis. Comput Methods Appl Mech Eng 354:245–270
45. De Berg M, Van Kreveld M, Overmars M, Schwarzkopf OC (2000) Computational geometry. Springer, Berlin

46. Zhang P, Karimpour M, Balint D, Lin J (2012) Three-dimensional virtual grain structure generation with grain size control. Mech Mater 55:89–101
47. Boots B (1982) The arrangement of cells in "random" networks. Metallography 15:53–62
48. Aboav D (1970) The arrangement of grains in a polycrystal. Metallography 3:383–390
49. Groeber MA, Jackson MA (2014) DREAM: 3D: A digital representation environment for the analysis of microstructure in 3D. Integrating Materials and Manufacturing Innovation 3:5
50. Chen L-Q (2002) Phase-field models for microstructure evolution. Annu Rev Mater Res 32:113–140
51. Rollett A, Raabe D (2001) A hybrid model for mesoscopic simulation of recrystallization. Comput Mater Sci 21:69–78
52. Rollett AD (1997) Overview of modeling and simulation of recrystallization. Prog Mater Sci 42:79–99
53. Raabe D (1999) Introduction of a scalable three-dimensional cellular automaton with a probabilistic switching rule for the discrete mesoscale simulation of recrystallization phenomena. Philos Mag A 79:2339–2358
54. Marx V, Reher FR, Gottstein G (1999) Simulation of primary recrystallization using a modified three-dimensional cellular automaton. Acta Mater 47:1219–1230
55. Spowart JE, Mullens HE, Puchala BT (2003) Collecting and analyzing microstructures in three dimensions: a fully automated approach. JOM 55:35–37
56. Spowart JE (2006) Automated serial sectioning for 3-D analysis of microstructures. Scr Mater 55:5–10
57. Zaafarani N, Raabe D, Singh R, Roters F, Zaefferer S (2006) Three-dimensional investigation of the texture and microstructure below a nanoindent in a Cu single crystal using 3D EBSD and crystal plasticity finite element simulations. Acta Mater 54:1863–1876
58. Calcagnotto M, Ponge D, Demir E, Raabe D (2010) Orientation gradients and geometrically necessary dislocations in ultrafine grained dual-phase steels studied by 2D and 3D EBSD. Mater Sci Eng, A 527:2738–2746
59. Khorashadizadeh A, Raabe D, Zaefferer S, Rohrer G, Rollett A, Winning M (2011) Five-parameter grain boundary analysis by 3D EBSD of an ultra fine grained CuZr alloy processed by equal channel angular pressing. Adv Eng Mater 13:237–244
60. Zaefferer S, Wright S, Raabe D (2008) Three-dimensional orientation microscopy in a focused ion beam–scanning electron microscope: a new dimension of microstructure characterization. Metall Mater Trans A 39:374–389
61. Yi S, Schestakow I, Zaefferer S (2009) Twinning-related microstructural evolution during hot rolling and subsequent annealing of pure magnesium. Mater Sci Eng A 516:58–64
62. Uchic MD, Groeber MA, Dimiduk DM, Simmons JP (2006) 3D microstructural characterization of nickel superalloys via serial-sectioning using a dual beam FIB-SEM. Scr Mater 55:23–28
63. Li SF, Lind J, Hefferan CM, Pokharel R, Lienert U, Rollett AD, Suter RM (2012) Three-dimensional plastic response in polycrystalline copper via near-field high-energy X-ray diffraction microscopy. J Appl Crystallogr 45:1098–1108
64. Lind J, Li SF, Pokharel R, Lienert U, Rollett AD, Suter RM (2014) Tensile twin nucleation events coupled to neighboring slip observed in three dimensions. Acta Mater 76:213–220
65. Stein CA, Cerrone A, Ozturk T, Lee S, Kenesei P, Tucker H, Pokharel R, Lind J, Hefferan C, Suter RM, Ingraffea AR, Rollett AD (2014) Fatigue crack initiation, slip localization and twin boundaries in a nickel-based superalloy. Curr Opin Solid State Mater Sci 18:244–252
66. Ludwig W, Schmidt S, Lauridsen EM, Poulsen HF (2008) X-ray diffraction contrast tomography: a novel technique for three-dimensional grain mapping of polycrystals. I. Direct beam case. J Appl Crystallogr 41:302–309
67. Johnson G, King A, Honnicke MG, Marrow J, Ludwig W (2008) X-ray diffraction contrast tomography: a novel technique for three-dimensional grain mapping of polycrystals. II. The combined case. J Appl Crystallogr 41:310–318
68. Qidwai SM, Turner DM, Niezgoda SR, Lewis AC, Geltmacher AB, Rowenhorst DJ, Kalidindi SR (2012) Estimating the response of polycrystalline materials using sets of weighted statistical volume elements. Acta Mater 60:5284–5299
69. Choi YS, Groeber MA, Turner TJ, Dimiduk DM, Woodward C, Uchic MD, Parthasarathy TA (2012) A crystal-plasticity FEM study on effects of simplified grain representation and mesh types on mesoscopic plasticity heterogeneities. Mater Sci Eng, A 553:37–44
70. Knezevic M, Drach B, Ardeljan M, Beyerlein IJ (2014) Three dimensional predictions of grain scale plasticity and grain boundaries using crystal plasticity finite element models. Comput Methods Appl Mech Eng 277:239–259
71. Barrett TJ, Savage DJ, Ardeljan M, Knezevic M (2018) An automated procedure for geometry creation and finite element mesh generation: application to explicit grain structure models and machining distortion. Comput Mater Sci 141:269–281
72. Ardeljan M, Knezevic M, Nizolek T, Beyerlein IJ, Mara NA, Pollock TM (2015) A study of microstructure-driven strain localizations in two-phase polycrystalline HCP/BCC composites using a multi-scale model. Int J Plast 74:35–57
73. Knezevic M, Daymond MR, Beyerlein IJ (2016) Modeling discrete twin lamellae in a microstructural framework. Scr Mater 121:84–88
74. Wang S, Zhuang W, Cao J, Lin J (2010) An investigation of springback scatter in forming ultra-thin metal-sheet channel parts using crystal plasticity FE analysis. Int J Adv Manuf Technol 47:845–852
75. Zhuang W, Wang S, Cao J, Lin J, Hartl C (2010) Modelling of localised thinning features in the hydroforming of micro-tubes using the crystal-plasticity FE method. Int J Adv Manuf Technol 47:859–865
76. Cubit https://cubit.sandia.gov/
77. Asaro RJ, Needleman A (1985) Texture development and strain hardening in rate dependent polycrystals. Acta Metall Mater 33:923–953
78. Hutchinson JW (1976) Bounds and self-consistent estimates for creep of polycrystalline materials. Proc R Soc Lond A 348:101–126
79. Zecevic M, Beyerlein IJ, McCabe RJ, McWilliams BA, Knezevic M (2016) Transitioning rate sensitivities across multiple length scales: microstructure-property relationships in the Taylor cylinder impact test on zirconium. Int J Plast 84:138–159
80. Kocks U, Argon A, Ashby M (1975) Progress in materials science. Thermodyn Kinet Slip 19:110–170
81. Beyerlein IJ, Tomé CN (2008) A dislocation-based constitutive law for pure Zr including temperature effects. Int J Plast 24:867–895
82. Madec R, Devincre B, Kubin L, Hoc T, Rodney D (2003) The role of collinear interaction in dislocation-induced hardening. Science 301:1879–1882
83. Knezevic M, Carpenter JS, Lovato ML, McCabe RJ (2014) Deformation behavior of the cobalt-based superalloy Haynes 25: experimental characterization and crystal plasticity modeling. Acta Mater 63:162–168
84. Knezevic M, McCabe RJ, Tomé CN, Lebensohn RA, Chen SR, Cady CM, Gray Iii GT, Mihaila B (2013) Modeling mechanical response and texture evolution of α-uranium as a function of strain rate and temperature using polycrystal plasticity. Int J Plast 43:70–84

85. Zecevic M, Knezevic M, Beyerlein IJ, McCabe RJ (2016) Texture formation in orthorhombic alpha-uranium under simple compression and rolling to high strains. J Nucl Mater 473:143–156
86. Knezevic M, Zecevic M, Beyerlein IJ, Bingert JF, McCabe RJ (2015) Strain rate and temperature effects on the selection of primary and secondary slip and twinning systems in HCP Zr. Acta Mater 88:55–73
87. Mecking H, Kocks UF (1981) Kinetics of flow and strain-hardening. Acta Metall Mater 29:1865–1875
88. Madec R, Devincre B, Kubin LP (2002) From dislocation junctions to forest hardening. Phys Rev Lett 89:255508
89. Eghtesad A, Knezevic M (2020) High-performance full-field crystal plasticity with dislocation-based hardening and slip system back-stress laws: application to modeling deformation of dual-phase steels. J Mech Phys Solids 134:103750
90. Lavrentev FF (1980) The type of dislocation interaction as the factor determining work hardening. Mater Sci Eng 46:191–208
91. Essmann U, Mughrabi H (1979) Annihilation of dislocations during tensile and cyclic deformation and limits of dislocation densities. Philos Mag A 40:731–756
92. Mughrabi H (1987) A two-parameter description of heterogeneous dislocation distributions in deformed metal crystals. Materials science and engineering 85:15–31
93. Jackson PJ (1985) Dislocation modelling of shear in f.c.c. crystals. Prog Mater Sci 29:139–175
94. Wang Z, Beyerlein I, LeSar R (2007) The importance of cross-slip in high-rate deformation. Modell Simul Mater Sci Eng 15:675
95. Peeters B, Bacroix B, Teodosiu C, Van Houtte P, Aernoudt E (2001) Work-hardening/softening behaviour of b.c.c. polycrystals during changing strain paths: II. TEM observations of dislocation sheets in an IF steel during two-stage strain paths and their representation in terms of dislocation densities. Acta Mater 49:1621–1632
96. Kocks UF, Mecking H (2003) Physics and phenomenology of strain hardening: the FCC case. Prog Mater Sci 48:171–273
97. Owen SJ, Brown JA, Ernst CD, Lim H, Long KN (2017) Hexahedral mesh generation for computational materials modeling. Procedia engineering 203:167–179
98. Owen SJ, Staten ML and Sorensen MC (2011) Parallel hex meshing from volume fractions. In: Proceedings of the 20th international meshing roundtable. Springer, pp 161–178
99. Allen SM, Cahn JW (1979) A microscopic theory for antiphase boundary motion and its application to antiphase domain coarsening. Acta Metall 27:1085–1095
100. Abdeljawad F, Foiles SM (2015) Stabilization of nanocrystalline alloys via grain boundary segregation: a diffuse interface model. Acta Mater 101:159–171
101. Abdeljawad F, Völker B, Davis R, McMeeking RM, Haataja M (2014) Connecting microstructural coarsening processes to electrochemical performance in solid oxide fuel cells: an integrated modeling approach. J Power Sources 250:319–331
102. Ardeljan M, Beyerlein IJ, Knezevic M (2017) Effect of dislocation density-twin interactions on twin growth in AZ31 as revealed by explicit crystal plasticity finite element modeling. Int J Plast 99:81–101
103. Ardeljan M, Knezevic M (2018) Explicit modeling of double twinning in AZ31 using crystal plasticity finite elements for predicting the mechanical fields for twin variant selection and fracture analyses. Acta Mater 157:339–354
104. (2013) Patran Version 2013, MSC Software Corporation, Newport Beach, CA, USA
105. (2017) ABAQUS Version 6, Dassault Systèmes, Providence, RI, USA

Terms and Conditions

Springer Nature journal content, brought to you courtesy of Springer Nature Customer Service Center GmbH (“Springer Nature”).
Springer Nature supports a reasonable amount of sharing of research papers by authors, subscribers and authorised users (“Users”), for small-scale personal, non-commercial use provided that all copyright, trade and service marks and other proprietary notices are maintained. By accessing, sharing, receiving or otherwise using the Springer Nature journal content you agree to these terms of use (“Terms”). For these purposes, Springer Nature considers academic use (by researchers and students) to be non-commercial.
These Terms are supplementary and will apply in addition to any applicable website terms and conditions, a relevant site licence or a personal subscription. These Terms will prevail over any conflict or ambiguity with regards to the relevant terms, a site licence or a personal subscription (to the extent of the conflict or ambiguity only). For Creative Commons-licensed articles, the terms of the Creative Commons license used will apply.
We collect and use personal data to provide access to the Springer Nature journal content. We may also use these personal data internally within ResearchGate and Springer Nature and as agreed share it, in an anonymised way, for purposes of tracking, analysis and reporting. We will not otherwise disclose your personal data outside the ResearchGate or the Springer Nature group of companies unless we have your permission as detailed in the Privacy Policy.
While Users may use the Springer Nature journal content for small scale, personal non-commercial use, it is important to note that Users may not:

1. use such content for the purpose of providing other users with access on a regular or large scale basis or as a means to circumvent access control;
2. use such content where to do so would be considered a criminal or statutory offence in any jurisdiction, or gives rise to civil liability, or is otherwise unlawful;
3. falsely or misleadingly imply or suggest endorsement, approval , sponsorship, or association unless explicitly agreed to by Springer Nature in writing;
4. use bots or other automated methods to access the content or redirect messages
5. override any security feature or exclusionary protocol; or
6. share the content in order to create substitute for Springer Nature products or services or a systematic database of Springer Nature journal content.

In line with the restriction against commercial use, Springer Nature does not permit the creation of a product or service that creates revenue, royalties, rent or income from our content or its inclusion as part of a paid for service or for other commercial gain. Springer Nature journal content cannot be used for inter-library loans and librarians may not upload Springer Nature journal content on a large scale into their, or any other, institutional repository.
These terms of use are reviewed regularly and may be amended at any time. Springer Nature is not obligated to publish any information or content on this website and may remove it or features or functionality at our sole discretion, at any time with or without notice. Springer Nature may revoke this licence to you at any time and remove access to any copies of the Springer Nature journal content which have been saved.
To the fullest extent permitted by law, Springer Nature makes no warranties, representations or guarantees to Users, either express or implied with respect to the Springer nature journal content and all parties disclaim and waive any implied warranties or warranties imposed by law, including merchantability or fitness for any particular purpose.
Please note that these rights do not automatically extend to content, data or other material published by Springer Nature that may be licensed from third parties.
If you would like to use or distribute our Springer Nature journal content to a wider audience or on a regular basis or in any other manner not expressly permitted by these Terms, please contact Springer Nature at

onlineservice@springernature.com